

Highlights

Future frame prediction in chest cine MR imaging using the PCA respiratory motion model and dynamically trained recurrent neural networks

Michel Pohl, Mitsuru Uesaka, Hiroyuki Takahashi, Kazuyuki Demachi, Ritu Bhusal Chhatkuli

- RNNs trained online can accurately forecast future frames in chest cine-MR imaging.
- Online learning helps adapt to unsteady motion and reach high accuracy with few data.
- Respiratory motion corresponded mainly to the first or second PCA component.
- Predicting higher-order PCA weights related with minor deformations boosted accuracy.
- Linear filters and RNNs estimated motion well at low and high horizons, respectively.

Future frame prediction in chest cine MR imaging using the PCA respiratory motion model and dynamically trained recurrent neural networks

Michel Pohl^{a,*}, Mitsuru Uesaka^b, Hiroyuki Takahashi^a, Kazuyuki Demachi^a and Ritu Bhusal Chhatkuli^c

^aThe University of Tokyo, 113-8654 Tokyo, Japan

^bJapan Atomic Energy Commission, 100-8914 Tokyo, Japan

^cNational Institutes for Quantum and Radiological Science and Technology, 263-8555 Chiba, Japan

ARTICLE INFO

Keywords:

radiotherapy
video prediction
recurrent neural network
online learning
principal component analysis

ABSTRACT

Lung tumors follow the respiratory motion and are thus difficult to target accurately during radiotherapy. Not considering the latency of treatment systems may lead to uncertainty in the estimated tumor location and high irradiation of healthy tissue surrounding it. This work addresses the challenge of future frame prediction in chest dynamic magnetic resonance (MR) image sequences to compensate for the time delay using recurrent neural networks (RNN) trained with online learning algorithms. The latter enable networks to adapt to the changing respiratory patterns of each patient and help mitigate irregular movements unseen in the training set, as they update synaptic weights with each new training example.

Experiments were conducted using four publicly available two-dimensional (2D) thoracic cine-magnetic resonance imaging (MRI) sagittal sequences of volunteers sampled at 3.18Hz. Principal component analysis (PCA) decomposes the time-varying displacement vector field (DVF), computed using the pyramidal Lucas-Kanade optical flow algorithm, into static deformation fields and low-dimensional time-dependent weights. We compare various algorithms to forecast the latter: linear regression, least mean squares (LMS), and RNNs trained with real-time recurrent learning (RTRL), unbiased online recurrent optimization (UORO), decoupled neural interfaces (DNI) and sparse 1-step approximation (SnAp-1). Predicting the DVF projection onto the linear PCA feature subspace enables estimating the deformation field in the future and, in turn, the next frames by warping the initial image.

Linear regression led to the lowest mean predicted deformation error at a horizon $h = 0.32s$ (the time interval in advance for which the prediction is made), equal to 1.30mm, followed by SnAp-1 and RTRL, whose error increased from 1.37mm to 1.44mm as h increased from 0.62s to 2.20s. Similarly, the structural similarity index measure (SSIM) of LMS decreased from 0.904 to 0.898 as h increased from 0.31s to 1.57s and was the highest among the algorithms compared for the latter horizons. SnAp-1 attained the highest SSIM for $h \geq 1.88s$, with values of less than 0.898. The predicted images look similar to the original ones, and the highest errors occurred at challenging areas such as the diaphragm boundary at the end-of-inhale phase, where motion variability is more prominent, and regions where out-of-plane motion was more prevalent.

1. Introduction

1.1. Respiratory motion management in MR-guided radiotherapy

Machine learning can benefit external beam radiotherapy at various steps within the clinical workflow, ranging from supporting the optimal treatment plan selection, improving dose planning and radiation delivery, to helping assess patient response to the therapy session [1]. Respiratory motion forecasting during treatment is a critical application that can enhance therapeutic irradiation precision and patient outcome. Indeed, the beam may partially miss the moving target (e.g., the lung or pancreas tumor) and negatively affect surrounding healthy tissue instead, due to the intrinsic latency of the treatment system. Specifically, rotation, deformation, and translation of the tumor and surrounding organs at risks induced by breathing can cause geometric and dosimetric errors. Chest tumor motion is primarily periodic, with a range

in the cranio-caudal direction sometimes exceeding 5cm [2]. Nonetheless, it is influenced by phase shifts and local variations in frequency and amplitude. Amplitude shifts refer to sudden and occasional variations in the average position of the organs, while the term "drift" describes more gradual changes occurring during a single treatment session. As an example, baseline intrafractional drifts of 1.65 ± 5.95 mm, 1.50 ± 2.54 mm, and 0.45 ± 2.23 mm (mean \pm standard deviation) have been observed in the superior-inferior (SI), anterior-posterior, and left-right directions, respectively, in [3]. Moreover, general posture changes due to patient relaxation as time elapses or minor positional adjustments on the treatment bed also add to the variability in chest motion records. Each radiotherapy treatment system has a specific characteristic time delay, but "for most radiation treatments, the latency will be more than 100ms, and can be up to two seconds" [4].

During external beam radiotherapy treatment of chest tumors, the latter's three-dimensional (3D) volume cannot be imaged fully in real time. Conventional methods rely on

*Corresponding author

 michel.pohl@centrale-marseille.fr (M. Pohl)

tracking metallic fiducial markers implanted near the target using kilovoltage (kV) fluoroscopic imaging, which is unfortunately invasive, or external markers placed on the chest, which is more tolerable but limited by a low correlation with the target motion and the associated phase shift. Several works also proposed deriving internal motion from the whole chest surface imaged with optical cameras. The recent advancements in magnetic resonance imaging (MRI) technology enable observing soft tissue and organ motion in real-time in a fixed imaging plane with high contrast. Moreover, recent magnetic resonance (MR)-guided radiotherapy systems do not involve the burden of additional imaging dose, as opposed to kV fluoroscopy imaging or four-dimensional cone beam computed tomography (4D-CBCT) acquisitions. Because MRI is not subject to dose restrictions, free-breathing in the two-dimensional (2D) slice of interest featuring inter-cycle variations can be imaged for relatively long, as opposed to 4D-CBCT imaging, which can only capture an average breathing cycle. Fast four-dimensional (4D) MR acquisition is a current area of research, as the proposed 4D imaging techniques result in a relatively low spatial resolution and quality. In that context, MR-guided radiotherapy can benefit from artificial intelligence (AI) enhancements regarding 3D volume motion estimation from partial observations, and irradiation delay mitigation. Our work focuses on the latter point, but we will briefly cover advances concerning the former as they relate to the spatial motion model that we employed.

Much research has been conducted on exploring mathematical correspondence models that can derive 3D internal motion, which is not observable in real-time, from surrogate signals, also referred to as partial observations (in the case of imaging). Such models usually require a fitting procedure involving simultaneous image and surrogate signal acquisitions. As an example, liver motion recorded via ultrasound imaging was inferred from the position of light-emitting diodes (LED) placed on the chest surface of volunteers (AccuTrack 250 system) using a Long Short-Term Memory (LSTM) network in [5]. The latter was coupled with another LSTM forecasting the position of the LEDs to achieve spatio-temporal prediction. The authors found that LSTMs were more effective than support vector regression (SVR) at both tasks and that continuously updating the correlation model improved the accuracy. Correspondence models are referred to as subject-specific when the fitting procedure is performed using the data from a single patient or population-based when it involves data from several subjects.

Principal component analysis (PCA), an unsupervised dimensionality reduction algorithm that can be interpreted as fitting an ellipsoid to the data, has been a popular tool used to build correspondence models. One commonly performs eigendecomposition on a motion matrix constructed via deformable image registration (DIR) between a reference phase and other phases in a four-dimensional dataset (Appendix B). That approach implicitly assumes that linear combinations of the eigenvectors associated with the largest

eigenvalues can approximate every potential organ motion state. Two broad categories in using PCA for correspondence modeling are highlighted in [6]. In direct modeling, PCA is applied to internal or surrogate data, in which case a regression method is fitted using the PCA weights, or PCA is used to fit the correspondence model. The first article introducing the PCA respiratory motion model belongs to the latter subcategory [7]. In that work, the displacement vector field (DVF) within the whole chest was inferred from the diaphragm position in four-dimensional computed tomography (4DCT) images; it was observed that two principal components were sufficient to describe the breathing motion accurately. Another example where PCA is used to fit the correspondence model is the work of Chen et al., where the tumor and lung motion is derived from the external chest surface using 4DCT imaging with a particle-based surface meshing approach and topology preserving non-rigid point matching registration algorithm [8]. By contrast, in indirect models, the weights associated with the principal components derived from internal motion are estimated using numerical optimization by maximizing the similarity between the partial observations and the corresponding 2D cross-sections from the inferred 3D data. For instance, subject-specific indirect models were used to estimate volumetric MR scans from 2D cine-MRI in [9, 10]. In those two studies, iterative optimization of the weights of the eigenvectors was conducted until satisfactory alignment between the observed 2D cross-sections and warped reference volume was reached. Romaguera et al. mentioned that "results reported for these patient-specific models are often more accurate than for population-based methods. In a clinical scenario, their reliability depends, however, on the degree of patient-specific inter-fraction motion variations."

1.2. Respiratory motion forecasting with dynamically trained RNNs

Recurrent connections are widespread in recent artificial neural network (ANN) architectures proposed for respiratory motion forecasting in radiotherapy [12, 13, 14, 15]. Indeed, the feedback loop at the core of diverse recurrent neural network (RNN) models acts as a form of memory, enabling the storage and retrieval of information over time. This distinctive feature allows these networks to effectively learn patterns and relationships within sequential data and surpass conventional multilayer perceptrons (MLP) in time series or natural language processing. One training strategy consists of adjusting the network weights as new incoming samples become available to better handle unique breathing patterns not previously encountered in the training set. A straightforward method to achieve that involves retraining the network as new data points are obtained using a sliding time interval window beyond which past data is discarded. For instance, such an approach was previously used to dynamically retrain LSTMs forecasting the SI component of the tumor center of mass in 2D cine-MR sequences and adapt a population model to a specific patient [16]. The authors reported a root-mean-square error (RMSE) decrease from 2.02mm to

1.77mm and from 1.59mm to 1.34mm on the two test sets that they used when dynamically retraining the LSTM with a horizon (the time interval in the future for which the prediction is made, also called response time or look-ahead time) equal to $h = 750\text{ms}$ compared to offline learning (i.e., not performing adaptation). That strategy can enhance performance, but it has a significant drawback: with each new retraining cycle, the algorithm progressively forgets the characteristics of earlier data that fall outside the new window. A very similar and conventional way of training RNNs is truncated backpropagation through time (TBPTT); while being relatively resource-efficient with a complexity of $\mathcal{O}(q^2)$, where q denotes the number of hidden units, it suffers from a bias towards more recent dependencies [17].

Unlike dynamic retraining with a sliding window approach or TBPTT, truly online training methods retain learned knowledge over a longer time span. Indeed, the corresponding equations governing the update of the network parameters do not directly reference a time point in the past beyond which information is lost. Real-time recurrent learning (RTRL), a fundamental online learning algorithm for RNNs, operates by recursively updating the sensitivity matrix (the derivative of the hidden state with respect to the parameters), also referred to as the influence matrix, at each time step [18]. It has previously been applied to the forecast of the locations of fiducial markers implanted in the lungs (SyncTraX system) [19], abdominal and thoracic cancer lesions recorded by CyberKnife Synchrony system [20], chest internal points tracked with DIR in 4D cone beam computed tomography (CBCT) images [21], as well as external markers placed on the abdomen and chest of healthy volunteers (NDI Polaris system) [22, 23]. Nonetheless, RTRL is limited by its high computational complexity, which scales as $\mathcal{O}(q^4)$, rendering inference impractical even for moderately sized networks.

Several algorithms for online training of RNNs were recently proposed as an attempt to lower computational requirements compared to RTRL while avoiding bias in the loss gradient estimation, as introduced in TBPTT, as much as possible, effectively balancing short-term and long-term signal dependencies (cf for instance the discussion in [24]). One is unbiased online recurrent optimization (UORO), which approximates the sensitivity matrix as the product of two random vectors updated recursively at each time step, using the "rank-one trick" [25]. UORO produces unbiased gradient estimates using a closed-form update rule, albeit with the trade-off of introducing stochasticity. Other approaches seek to reduce time complexity by leveraging sparsity, such as sparse n -step approximation (SnAp- n), which only monitors the effect of weights on hidden units impacted within n steps of the recurrent core [26]. Although the latter algorithm introduces a bias in the loss gradient computation, it maintains a non-stochastic closed-form update. The specific case $n = 1$, sparse 1-step approximation (SnAp-1), is equivalent to a diagonal approximation of the sensitivity matrix analogous to that proposed in the original LSTM paper [27]. In opposition to UORO and SnAp-1, which attempt to

compress the information in the sensitivity matrix, decoupled neural interfaces (DNI) is a future-facing algorithm; in other words, it relies on error signal prediction. Originally introduced as a versatile framework relevant to both recurrent and non-recurrent networks, DNI seeks to eliminate the dependency of network modules on the completion of backward or forward computations by other modules before the update of their own weights. That is achieved by learning a "synthetic gradient," an independent estimate of the loss gradient at each layer. DNI's gradient updates are biased, deterministic, and numerical since there is no closed-form expression to directly compute the error signal, necessitating a gradient descent step instead. UORO, SnAp-1, and DNI all benefit from a computational complexity of $\mathcal{O}(q^2)$ lower than that of RTRL. Efficient implementations of these three algorithms for vanilla RNNs were proposed in [22, 23]. In the latter works, they are applied for the first time to radiotherapy by forecasting the position of external markers and demonstrated higher performance than RTRL; the hidden layer size was reduced when using RTRL to compensate for the latter's high processing time.

1.3. Future frame forecasting in natural and thoracic video sequences

Similar to time series forecasting, video prediction, the self-supervised task of estimating future frames given a sequence of past successive frames, has seen much interest in the computer vision community, with some applications in robotic control [28], autonomous driving [29, 30, 31], or precipitation nowcasting [32]. Forecasting natural images is challenging as those are characterized by complex pixel dynamics at different scales, subject to occlusions, camera motion, or variations in lighting conditions. Furthermore, the future is multimodal, as there are generally multiple equally plausible future outcomes given the information in the past frames. That phenomenon experimentally results in blurry predictions, especially when the horizon is high. More generally, it was observed that forecasting frames further in the future tends to lead to less accurate results. Due to their high capabilities in sequential data processing, RNNs are often used as the temporal modeling backbone of video forecasting architectures. Early works focusing specifically on these include the introduction of the convolutional LSTM [32], which is more suited to the image space than its classical counterpart, and the extension of the LSTM-based encoder-decoder framework, originally developed for machine translation [33], to video prediction [34]. Dynamic retraining, i.e., periodically fine-tuning the network in the inference phase, was applied to video forecasting in [29], which improved accuracy for long-term predictions.

Oprea et al. comprehensively surveyed deep learning methods for video prediction and categorized them as follows [35]. Initial approaches attempted to forecast raw pixel values straightforwardly, aiming to implicitly capture fine details and scene dynamics [32, 34, 30]. Nevertheless, learning an appropriately stable and meaningful representation from raw frames proved difficult due to the high dimension-

ality and variability of the pixel space. That challenge led to developments aimed at reducing the dimensionality of internal representations and supervision complexity. On the one hand, some works focused on separating variability elements from the visual content, which Oprea et al. refer to as "factorizing the prediction space." One such strategy consists of disentangling motion and appearance using a two-stream processing approach [36]. Another subcategory encompasses methods that model variability factors as explicit transformations between subsequent frames to leverage the latter's high level of similarity, using kernel-based or vector-based resampling [37, 38]. The latter consists of predicting a DVF and applying it to one of the observed frames to generate the estimated future frame. It generally relies on the spatial transformer network (STN), a module that learns to perform geometrical transformations on an input image or feature map [39]. It was argued that vector-based resampling approaches "can avoid [the] blurring problem by copying coherent regions of pixels from existing frames" and "lead to more realistic and sharper results than techniques that hallucinate pixels from scratch" [38]. On the other hand, Oprea et al. group together methods that "narrow the prediction space" either by "conditioning the predictions on extra variables," such as the robot state and action [37, 40], or redefining the forecasting task in a higher-level space, such as semantic or instance segmentation maps [29, 31], or keypoint coordinates [28]. In parallel to works focused on simplifying the prediction task, other research efforts have also tackled the challenge of future multimodality by proposing algorithms based on probabilistic models such as variational auto-encoders (VAE) [40, 41, 28]. A VAE compresses and recovers the input x to capture a low-dimensional representation z that encapsulates the most significant factors of variability in x . When applied to image generation, VAEs seek to produce new images by sampling from a prior distribution over the latent encoding z , thus introducing a probabilistic element to traditional autoencoders' otherwise deterministic latent space.

Video prediction using dynamic chest imaging is valuable for radiotherapy, as it helps characterize the complete deformation of the moving target. By contrast, most previous works on tumor position estimation attempted to predict only its center of mass, whose sole trajectory is an incomplete representation of motion. In chest MR scan sequence prediction, multimodality can appear in the form of respiratory and cardiac irregularities or out-of-plane motion (Section 1.1). Furthermore, a low signal-to-noise ratio (SNR) caused by a weak magnetic field and distortions or degradations due to susceptibility, flow, chemical shift, or magnetic field inhomogeneity artifacts can make prediction more difficult. The relatively low acquisition frequency and amount of data for training in available cine-MR chest scan datasets are additional challenges specific to medical imaging. Chhatkuli et al. proposed the first next-frame forecasting algorithm for chest video sequences, consisting of applying PCA to raw pixel intensities and predicting the time-dependent weights with multi-channel singular spectral analysis (MSSA) [42].

That method was validated using chest phantom kV fluoroscopic images and coronal slices from 4DCT acquisitions. Likewise, volumetric chest cine-MR scan sequences from extended cardiac-torso phantom (XCAT) data and an actual liver cancer patient were predicted by conducting PCA using the DVF between a reference frame and the current frame and forecasting the corresponding weights using MLPs combined with adaptive boosting in [43]. Although not strictly related to next-frame forecasting, a similar approach was used in [44] to predict chest surfaces reconstructed from point clouds captured by a 3D photogrammetry system. In that work, kernel PCA was applied to the surface height map, and a vector autoregressive model estimated the future low-dimensional time-varying representations in the kernel feature space. The PCA models in [42, 43, 44] were subject-specific, and it was observed that an oscillatory pattern following the breathing motion characterized the weights corresponding to the first principal components. The predictive coding network, a deep neural network design based on convolutional LSTMs and inspired by the neuroscience concept of predictive coding, was used to predict 2D cross-sections from chest 4DCT acquisitions as a direct pixel synthesis model in [45]. By contrast, Romaguera et al. used a vector-based resampling approach to forecast 2D liver images acquired using multiple modalities (MRI, computed tomography [CT], and ultrasound) [46]. The proposed algorithm was a modified version of VoxelMorph, an encoder-decoder neural network architecture for self-supervised DIR based on the STN module, including multi-scale residual blocks and ConvLSTMs for temporal prediction. Recent works have focused on future volumetric MR scan estimation from real-time 2D cine-MR acquisitions to simultaneously address the delays and real-time 3D imaging limitations of MR linear accelerator (LINAC) systems. First, an encoder-decoder architecture similar to that in [46], whose future latent encoding of the deformations is estimated from the incoming 2D frames, was proposed in [11]. The latter architecture was later reformulated using a (probabilistic) conditional VAE backbone, and the resulting network achieved a lower target (vessel) tracking error [47]. Further accuracy improvements were reported by replacing the ConvLSTMs in the latter work with a transformer architecture using prior-based conditioning and learnable queries for temporal prediction [48]. In general, it was documented that the predicted frames, especially at the diaphragm edge region, were less accurate around the end-inhale phase since the latter was subject to high inter-cycle variability. It was also reported that blood vessels appearing suddenly due to out-of-plane movement may not appear in the predictions [46].

1.4. Content of this study

This research is the first to apply online learning algorithms for RNNs, namely RTRL, UORO, SnAp-1, and DNI, to chest cine-MR image prediction and even video prediction in general, to the best of our knowledge. The forecasting model is specific to a given scan sequence: training and validation use the same video. PCA is applied to time-dependent

DVFs estimated using the pyramidal Lucas-Kanade optical flow algorithm to derive a subject-specific internal respiratory motion model. We forecast the time-varying PCA coefficients to obtain the embeddings corresponding to the next video frames. As such, our approach belongs to the vector-based resampling category in the classification of video forecasting models of Oprea et al. [35]. Our one-shot approach (i.e., not using a population model) produces satisfactory visual results and reaches numerical accuracy metrics similar to those previously reported in the literature about chest scan sequence prediction. That can be attributed to the capabilities of online learning algorithms to quickly adapt to new incoming data, corresponding potentially to irregular breathing. Additionally, PCA is a simple method that brings interpretability, as one can visualize how the prediction of a specific one-dimensional time-varying PCA weight translates into the deformation space. Our study is the first to determine the optimal number of components by cross-validation among the works in chest video prediction. Furthermore, our research is the first to utilize public cine-MR data for medical chest image sequence forecasting. To our knowledge, the MR records used are also longer (i.e., the number of time steps is higher) than those used in similar previous works; some comprise heart motion. Lastly, we compare the performance of RNNs, least mean squares (LMS), and linear regression for various horizons and accuracy measures and provide insights regarding hyper-parameter optimization for UORO, SnAp-1, and DNI.

2. Material and methods

2.1. Chest image data

This study uses two volumetric chest MR image sequences from an online public dataset [49]. The original 4D-MRI data were acquired using a technique based on “stacking of dynamic 2D images using internal image-based sorting” [50, 51]. Using bicubic spline interpolation, we resampled the original 3D volumes so that each voxel corresponds to a $1\text{mm} \times 1\text{mm} \times 1\text{mm}$ resolution. We then selected two sagittal cross-sections for each subject, totaling four sequences of 2D cross-sections. The 2D images thus have a spatial resolution of 1mm^2 per pixel and are encoded in 8 bits. Lastly, we shifted them such that the first image of each sequence corresponds to the middle phase within the expiration process. The resulting cine-MR sagittal sequences comprise each $M = 200$ frames (as the initial 4D data); Table 1 summarizes their characteristics. Sequences 1 and 4 comprise cross-sections from the left part of the chest and include cardiac motion, whereas sequences 2 and 3 correspond to the right hemithorax. Fig. 14 displays the mean image associated with each $2D+t$ sequence.

2.2. Breathing motion modeling with PCA

Given each MR image sequence, DIR between the initial 2D frame (at time t_1) and that at time t is performed using the pyramidal iterative Lucas-Kanade optical flow algorithm [52, 53], following the practical implementation in

Sq. index	Field of view (mm)	Pixel size (mm)	Sampling frequency	Nb. of frames	Breathing cycles	Heart visible?
1	270×270	1×1	3.22 Hz	200	14	Yes
2	270×270	1×1	3.22 Hz	200	14	No
3	290×290	1×1	3.15 Hz	200	28	Yes
4	290×290	1×1	3.15 Hz	200	28	No

Table 1

Characteristics of the dynamic chest MRI scan sequences

[22] (with a straightforward adaptation from 3D to 2D). The optical flow parameters are optimized with grid search: we select those that minimize the mean of the registration error over the first 90 images (details in Appendix A). In the following, we denote by $\vec{u}(\vec{x}, t)$ the push-forward 2D local deformation vector at pixel \vec{x} and time t , which satisfies the local brightness constancy assumption by definition:

$$I(\vec{x}, t_1) \approx I(\vec{x} + \vec{u}(\vec{x}, t_k), t_k) \quad (1)$$

The vector resulting from concatenating (and centering) the deformations $\vec{u}(\vec{x}, t)$ at time t , $X_c(t)$, lies in a high-dimensional space of dimension $2|I|$, where $|I|$ is the number of pixels (Eq. 25). However, the complex overall spatiotemporal variations are driven by relatively simple phenomena that can be described with few degrees of freedom. This work uses PCA to project the high-dimensional motion vector $X_c(t)$ onto a low-dimensional linear space. Mathematically, given an arbitrary number of principal components $n_{cp} \in \mathbb{N}$, for each $j \in \llbracket 1, \dots, n_{cp} \rrbracket$, we compute the j^{th} principal component $(\vec{u}_j(\vec{x}))_{\vec{x} \in I}$ and associated weights $(w_j(t_k))_{k \in \llbracket 1, \dots, M \rrbracket}$, which satisfy the following approximate relationship for all pixels \vec{x} at any time t :

$$\vec{u}(\vec{x}, t) \approx \vec{\mu}(\vec{x}) + \sum_{j=1}^{n_{cp}} w_j(t) \vec{u}_j(\vec{x}) \quad (2)$$

The formula above expresses the high-dimensional time-dependent DVF, $\vec{u}(\vec{x}, t)$, as a linear combination of a few (static) vector fields $\vec{u}_j(\vec{x})$ weighted by time-dependent signals $w_j(t)$. This article refers to the $\vec{u}_j(\vec{x})$ vectors as the principal DVFs. In Eq. 2, $\vec{\mu}(\vec{x})$ represents the (temporal) mean of $\vec{u}(\vec{x}, t_k)$ over $k \in \llbracket 1, \dots, M_{train} \rrbracket$, and the principal components $\vec{u}_j(\vec{x})$ are computed using the first M_{train} images of each sequence. To estimate the weights at time t_k when $k \geq M_{train}$, we project the centered DVF vector $X_c(t_k)$ onto the principal components, as described by Eq. 3. We set $M_{train} = 90$, except when performing prediction with linear regression, in which case $M_{train} = 160$ (the reason is explained in the next section).

$$w_j(t) = \sum_{\vec{x} \in I} \langle \vec{u}(\vec{x}, t) - \vec{\mu}(\vec{x}), \vec{u}_j(\vec{x}) \rangle \quad (3)$$

In the equation above, $\langle \cdot, \cdot \rangle$ designates the Euclidean inner product, and the sum is over all the pixels \vec{x} in the incoming image at time t . The principal components stay constant throughout each sequence since the motion model is

not updated as time elapses. This is a deliberate choice, as we assume that the breathing dynamics remain relatively stable within all sequences. Given that the latter are relatively short, around two minutes, and show no significant changes in motion patterns, we believe this is acceptable. Eq. 3 can easily be derived from Eq. 2 using the orthonormality of the vectors formed by the concatenation of the $\vec{u}_j(\vec{x})$ for $\vec{x} \in I$ in $\mathbb{R}^{2|I|}$:

$$\sum_{\vec{x} \in I} \langle \vec{u}_i(\vec{x}) | \vec{u}_j(\vec{x}) \rangle = \begin{cases} 1 & \text{if } i = j \\ 0 & \text{otherwise} \end{cases} \quad (4)$$

Appendix B contains further mathematical details concerning the derivation of Eqs. 2 and 3 from a linear algebra viewpoint.

2.3. Prediction of the time-dependent PCA weights

Predicting the following images is accomplished via forecasting the weights $w_j(t_k)$. We compare various prediction techniques: offline multivariate linear regression, LMS, and vanilla RNNs (also referred to as standard RNNs) with a single hidden layer trained online. The latter architecture can mathematically be described as follows:

$$x_{n+1} = \Phi(W_{a,n}x_n + W_{b,n}u_n) \quad y_{n+1} = W_{c,n}x_{n+1} \quad (5)$$

In the equations above, $W_{a,n}$, $W_{b,n}$, and $W_{c,n}$ refer respectively to the core-to-core, input-to-core, and core-to-output synaptic weights. Their shape is $q \times q$, $q \times (m+1)$, and $p \times q$, where m , p , and q denote respectively the input, output, and hidden layer sizes. These matrices depend on the time step index n , as online learning algorithms update them continually. Φ is the non-linear activation function; we set it as the coordinate-wise hyperbolic tangent function in this work. The RNN training algorithms that we selected for this study are respectively RTRL, UORO, SnAp-1, and DNI. Their implementation is the same as in [22, 23], which provide more technical details.

The input u_n of the forecasting algorithms consists of the concatenation of the weights $w_j(t_n), \dots, w_j(t_{n+L-1})$ for each component index $j \in \llbracket 1, \dots, n_{cp} \rrbracket$, where L designates the signal history length (SHL) expressed in number of time steps. The weights $w_1(t), \dots, w_{n_{cp}}(t)$ are predicted simultaneously to utilize temporal correlation information, thereby potentially increasing accuracy. The output vector y_{n+1} consists of the PCA weights at time $t_{n+L+h-1}$, where h refers to the horizon value expressed in number of time steps (Eq. 6). In our work, we study the influence of $h \in \llbracket 1, \dots, 7 \rrbracket$ on the prediction accuracy.

$$u_n = \begin{pmatrix} 1 \\ w_1(t_n) \\ w_2(t_n) \\ \dots \\ w_{n_{cp}}(t_n) \\ w_1(t_{n+1}) \\ \dots \\ w_{n_{cp}}(t_{n+L-1}) \end{pmatrix} \quad y_{n+1} = \begin{pmatrix} w_1(t_{n+L+h-1}) \\ \dots \\ w_{n_{cp}}(t_{n+L+h-1}) \end{pmatrix} \quad (6)$$

Each incoming input vector u_n is normalized by substituting it with $(u_n - \mu_{train}) / \sigma_{train}$ (the division is performed element-wise), where μ_{train} and σ_{train} are, respectively, the mean and standard deviation of the u_n s of the training set. That accelerates the convergence of stochastic gradient descent. The output y_{n+1} is then scaled back to the original space by replacing it with $\sigma_{train} * (y_{n+1} + \mu_{train})$, where $*$ refers to the element-wise multiplication. The loss gradient associated with the RNN or LMS is clipped when the latter is greater than $\tau_{RNN} = 100.0$ or $\tau_{LMS} = 2.0$, respectively, to ensure numerical stability [54]. The synaptic weights of the RNNs were initialized according to a Gaussian distribution of mean 0 and standard deviation $\sigma_{init} = 0.02$.

Learning is performed using only information from a single video used then for testing. Indeed, we do not build a generalized model but a sequence-specific model. Each time series is split into a training and development set of 56.3s and the remaining test set of 6.3s. The training set comprises the data between 0s and 28.3s, corresponding to $M_{train} = 90$ frames, except in the case of linear regression, where we set $M_{train} = 160$ because using more training data is beneficial to offline methods².

During cross-validation, we optimize the SHL for all the algorithms considered, the learning rate of the adaptive algorithms (LMS and RNNs), and the number of RNN hidden units (Table 2). The cross-validation set corresponds to the time indices $k \in \llbracket M_{train} + 1, \dots, M_{cv} \rrbracket$, where we set $M_{cv} = 180$ for all the forecasting methods considered. We select the hyper-parameters in the grid that minimize the normalized root-mean-square error (nRMSE) of the cross-validation set, defined in Eq. 7 (with $k_{min} = M_{train} + 1$ and $k_{max} = M_{cv}$).

$$nRMSE = \sqrt{\frac{\sum_{k=k_{min}}^{k_{max}} \sum_{j=1}^{n_{cp}} (w_j^{pred}(t_k) - w_j^{true}(t_k))^2}{\sum_{k=k_{min}}^{k_{max}} \sum_{j=1}^{n_{cp}} (\overline{w_j^{true}} - w_j^{true}(t_k))^2}} \quad (7)$$

In that equation, for each component order $j \in \llbracket 1, \dots, n_{cp} \rrbracket$, $w_j^{true}(t_k)$ designates the "ground-truth" time-dependent weight at time t_k computed by projecting the deformations associated with the incoming image onto the principal DVFs according to Eq. 3, $w_j^{pred}(t_k)$ the predicted weight at time t_k , and $\overline{w_j^{true}}$ the mean of $w_j^{true}(t_k)$ for $k \in \llbracket k_{min}, \dots, k_{max} \rrbracket$.

2.4. Image prediction

Given the predicted PCA weights, we estimate the future DVFs using Eq. 2. By doing so, we assume that the predicted motion always lies in the n_{cp} -dimensional linear

¹The matrices W and W_n of size $p \times (m+1)$ correspond to the linear regression and LMS coefficients, respectively. The latter depend on the time step index n since they are updated after receiving each new incoming sample, in opposition to the former. Similarly, the parameters W_a and W_b in the last row, corresponding to the RNN hidden layer, do not depend on n as the hidden units are considered frozen in that particular case (i.e., there is no update at any time step during inference).

²In particular, this means that the principal components and weights computed using linear regression differ from those associated with the adaptive methods (LMS and RNNs).

Prediction method	Mathematical model	Development set partition	Range of hyper-parameters for cross-validation
RTRL, UORO SnAp-1, DNI	$x_{n+1} = \Phi(W_{a,n}x_n + W_{b,n}u_n)$ $y_{n+1} = W_{c,n}x_{n+1}$	Training 28.3s Cross-validation 28.3s	$\eta \in \{0.005, 0.01, 0.015, 0.02\}$ $L \in \{6, 12, 18, 24, 30\}$ $q \in \{10, 30, 50, 70, 90, 110\}$
LMS	$y_{n+1} = W_n u_n$	Training 28.3s Cross-validation 28.3s	$\eta \in \{0.02, 0.05, 0.1, 0.2\}$ $L \in \{6, 12, 18, 24, 30\}$
Linear regression	$y_{n+1} = W u_n$	Training 50.3s Cross-validation 6.3s	$L \in \{6, 12, 18, 24, 30\}$
RNN with a frozen hidden layer	$x_{n+1} = \Phi(W_a x_n + W_b u_n)$ $y_{n+1} = W_{c,n} x_{n+1}$	Training 28.3s Cross-validation 28.3s	$\eta \in \{0.005, 0.01, 0.015, 0.02\}$ $L \in \{6, 12, 18, 24, 30\}$ $q \in \{10, 30, 50, 70, 90, 110\}$

Table 2

Overview of the forecasting techniques and cross-validation scheme considered in this research. The second column specifies the relationship between the input vector u_n containing the past PCA weights and the output vector y_{n+1} corresponding to the predicted weights (both defined in Eq. 6)¹. The fourth column outlines the hyper-parameter configuration employed for cross-validation using grid search, with η denoting the learning rate, L the SHL (expressed in number of time steps), and q the number of hidden units.

subspace spanned by the principal deformation fields. Fig. 1 illustrates the motion prediction problem from a geometrical viewpoint.

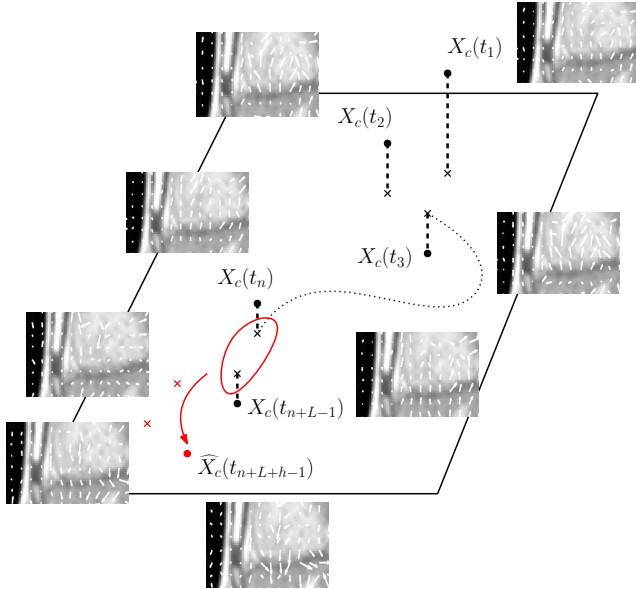


Figure 1: Geometrical interpretation of the motion prediction process. The flattened $2|I|$ -dimensional centered DVF at time t ($|I|$ denotes the number of pixels), $X_c(t)$, is projected onto the n_{cp} -dimensional linear subspace spanned by the (flattened) principal DVFs (Eq. 3). The predicted (flattened and centered) DVF at time $t_{n+L+h-1}$, $\widehat{X}_c(t_{n+L+h-1})$, lies on that linear subspace. This figure represents the case where $h = 3$, $L = 2$, and $n_{cp} = 2$.

The future frames are recovered by warping the initial image according to the predicted DVFs (Fig. 2). That implicitly relies on the assumptions that the motion field is reasonably smooth (i.e., mostly invertible) and that out-of-plane

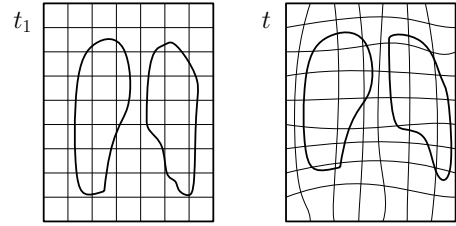


Figure 2: The chest image at time t is estimated by warping the initial image (at $t = t_1$)³.

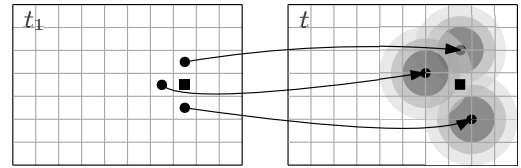


Figure 3: Warping the first image (at time $t = t_1$) using Nadaraya-Watson regression with a Gaussian kernel. The closer a point in the source image lands to the square point in the target image (at time t), the more it influences the intensity of that target pixel at t ⁴.

motion, artifacts, and brightness variations corresponding to the same tissue patch throughout the video are minimal. Since the intensity values are only known at locations with non-integer coordinates in the target frame, those values must be interpolated at the pixels with integer coordinates (i.e., on the conventional grid). To achieve that, we perform Nadaraya-Watson regression (Fig. 3), whose implementation in this work follows that in [21] (details can be found in the latter article).

The number of principal components n_{cp} is selected by

³Reprinted from [21], Copyright 2024, with permission from Elsevier.

⁴Same as footnote 3.

cross-validation. First, for each value of $n_{cp} \in \{1, 2, 3, 4\}$, the hyper-parameters that minimize the nRMSE of the cross-validation set (Eq. 7) are determined as described in Section 2.3. To select the optimal value of n_{cp} , we compute and maximize an accuracy metric quantifying the predicted vector field quality. We first define $\delta(\vec{u}, \vec{x}, t)$, the local instantaneous absolute registration error at pixel \vec{x} and time t , using the 4D vector field \vec{u} as follows:

$$\delta(\vec{u}, \vec{x}, t_k) = |I(\vec{x} + \vec{u}(\vec{x}, t_k), t_k) - I(\vec{x}, t_1)| \quad (8)$$

Using the latter quantity, one can calculate $\epsilon(\vec{u}, t_k)$, the instantaneous normalized registration RMSE at time t_k using the vector field \vec{u} :

$$\epsilon(\vec{u}, t_k) = \sqrt{\frac{\sum_{\vec{x}} \delta(\vec{u}, \vec{x}, t_k)^2}{\sum_{\vec{x}} (\bar{I}(t_1) - I(\vec{x}, t_1))^2}} \quad (9)$$

In that expression, $\bar{I}(t_1)$ designates the mean intensity of the initial image. Lastly, that latter error is evaluated using the vector field predicted using n_{cp} principal components, $\vec{u}^{(i)}(n_{cp})$ (i designates the run index), and averaged over the cross-validation time steps and evaluation runs (to take into account the stochasticity of the forecasting algorithms involved in the initialization or updates of the parameters):

$$E_{pred}(n_{cp}) = \frac{1}{n_{warp}(M_{cv} - M_{train})} \times \sum_{i=1}^{n_{warp}} \sum_{k=M_{train}+1}^{M_{cv}} \epsilon(\vec{u}^{(i)}(n_{cp}), t_k) \quad (10)$$

In this article, $E_{pred}(n_{cp})$ is referred to as the mean normalized registration RMSE. In the formula above, we select $n_{warp} = 25$ runs when evaluating RNN algorithms, except RTRL, for which we set $n_{warp} = 5$, as the latter is slower but experimentally yields error measurements with lower uncertainty. We choose the value of n_{cp} that minimizes $E_{pred}(n_{cp})$ (of the cross-validation set). That metric is relatively quick to compute, as it does not involve warping the initial image at t_1 . The overall image prediction pipeline and the main parameters involved are outlined in Fig. 4 and Table 7, respectively.

3. Results

3.1. Breathing motion modeling with PCA

The deformation vectors near the diaphragm mainly point upwards during expiration and downwards during inspiration (Fig. 5), following the lung tissue motion associated with breathing. Nonetheless, the entire displacement field does not homogeneously point up or down, as each organ moves and deforms in a specific way. Furthermore, artifacts and transverse motion causing sudden brightness variations led to relatively high fluctuations of the norm of the deformation vectors, for example, near the upper torso and lower back skin surface in sequence 1. Results regarding

the optimization of the DIR parameters can be found in Appendix A.

The first-order principal DVF of sequence 1 corresponds to the expansion and contraction of the right cardiac ventricle, as well as internal motion within the liver (Fig. 6). By contrast, the second principal DVF was mainly associated with respiratory motion, as the deformation vectors within the thoracic cavity tended to lean downwards uniformly. Notwithstanding, periodic intensity variations around the sternum and lumbar areas, primarily due to transversal motion, were captured by these two components. Likewise, in sequence 4, the first principal DVF corresponds to liver deformations and artifacts at the back area (Fig. 7). The spatial 2D vectors constituting the second-order principal component aligned upwards relatively homogeneously, reflecting the breathing motion.

In general, the time-dependent PCA weights appeared noisy and featured a certain level of instability. That may be due to various reasons, including the relatively low image acquisition frequency (3.18Hz). Indeed, the latter is unsuitable for properly visualizing high-frequency motion such as heart's, essentially characterized by $w_1(t)$ in sequence 1. The most regular and periodic component was the one associated with respiratory motion⁵. Specifically, the oscillations of $w_2(t)$ in sequence 4 had a higher frequency than $w_2(t)$ in sequence 1 because the breathing frequency in the former was higher than in the latter. In addition, the respiratory motion appeared more unsteady in sequence 4 than in sequence 1, which translates into higher amplitude variations in $w_2(t)$ in the former sequence compared to the latter. Nonetheless, the peaks of most components had some degree of synchronization, which suggests that PCA did not completely isolate respiratory motion in a single component.

The second PCA component in sequences 1, 3, and 4 primarily reflected the vertical mode of respiratory motion. In other words, PCA gave more importance to the rotational, compression, and expansion elements of breathing motion. As a result, forecasting only $w_1(t)$ in these sequences would likely not result in accurate respiratory motion prediction (more on that in Section 3.3). On the one hand, the principal components of order $j > 2$ also provide cues regarding the breathing motion and should thus not be neglected. For example, there was a strong correlation between the lower peaks of $w_3(t)$ and the associated peaks of $w_2(t)$ in Sequence 1. On the other hand, as the order j of the time-dependent weight $w_j(t)$ increased, the amplitude of the latter decreased, and those signals tended to become noisier and less predictable. Concomitantly, the amplitudes of the spatial components $\vec{u}_j(\vec{x})$ within the (air) background of the images tended to increase together with j . That happened as PCA attempts to "model" noise for high values of j . Disregarding components with a relatively high order j thus seems necessary to forecast future frames accurately.

⁵ $w_2(t)$ in sequence 1 (the component mainly associated with respiratory motion in that sequence) was very similar to $w_1(t)$ in sequence 2, even though the cross-sections looked different, because sequences 1 and 2 were extracted from the same 4D-MRI acquisition. Similarly, $w_1(t)$ and $w_2(t)$ in sequence 3 were similar to $w_1(t)$ and $w_2(t)$ in sequence 4, respectively.

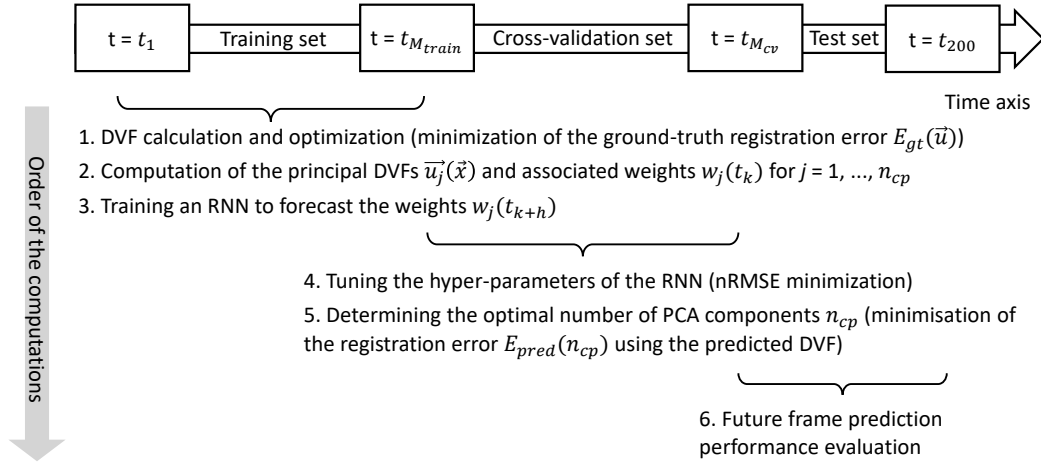
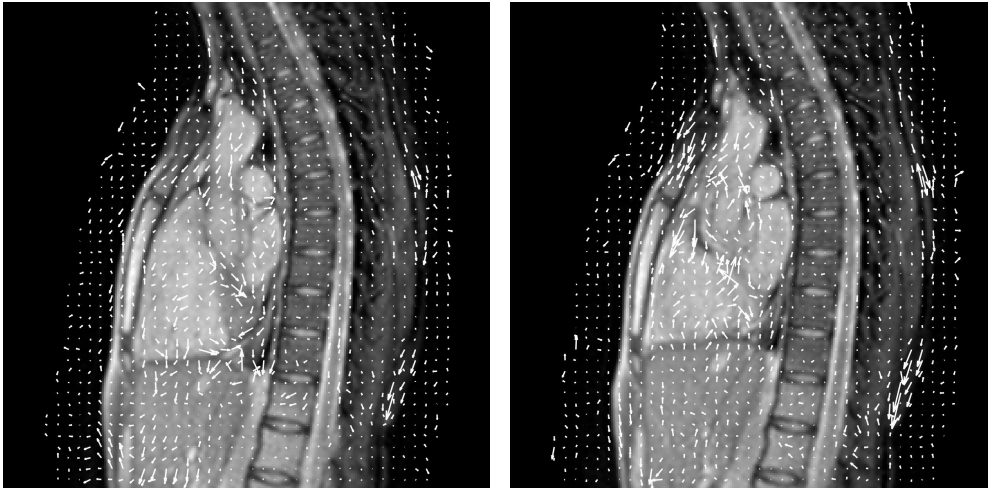


Figure 4: Overall experimental setting. We set $M_{train} = 90$ for each forecasting method, except linear regression, for which $M_{train} = 160$. The parameters of the optical flow algorithm used for DIR are optimized using the first 90 images. The cross-validation set ends at $t_{M_{cv}}$ with $M_{cv} = 180$.



(a) DVF between $t = t_1$ and $t = t_{28}$. The image at $t = t_{28}$ is displayed in the background. (b) DVF between $t = t_1$ and $t = t_{32}$. The image at $t = t_{32}$ is displayed in the background.

Figure 5: DVF in sequence 1 during inspiration (left) and expiration (right). The origins of each of the displayed 2D displacement vectors are separated from each other by 6 pixels (6mm). Best viewed with zoom-in on a digital display.

3.2. Prediction of the time-dependent weights

In this section only, we consider the case where the number of PCA components is fixed in advance and exclusively focus on the prediction of the time-dependent weights (steps 3 and 4 in Fig. 4). We arbitrarily set $n_{cp} = 3$ for the four sequences and compute the principal components associated with each sequence using the 90 first images⁶. Because the weights of the RNNs are initialized randomly, given each possible combination of hyper-parameters in the

⁶We used 160 images to compute the principal components when performing image prediction with linear regression (in Sections 3.3 and 3.4). However, in this section, we only use 90 images to calculate them when forecasting the time-dependent weights with linear regression, which we fit using 160 time steps, to compare the different algorithms using identical time-series sequences.

cross-validation range (Table 2), we average the nRMSE of the cross-validation set (Eq. 7 with $k_{min} = M_{train} + 1$ and $k_{max} = M_{cv}$) over $n_{cv} = 250$ successive runs; we select the hyper-parameter combination minimizing that error. In this section, we measure performance by averaging the nRMSE of the test set between the predicted and ground-truth time-dependent weights (Eq. 7 with $k_{min} = M_{cv} + 1$ and $k_{max} = 200$) over $n_{test}^{PCA} = 250$ evaluation runs. One exception is RTRL, for which we select $n_{cv} = n_{test}^{PCA} = 10$ because of its highest computational complexity. That value was acceptable in practice as RTRL was characterized by relatively low or moderate performance metric uncertainties, possibly due to the gradient computation exactness. By contrast, UORO and DNI were associated with larger confidence intervals (Table 3), which can be linked with the stochastic-

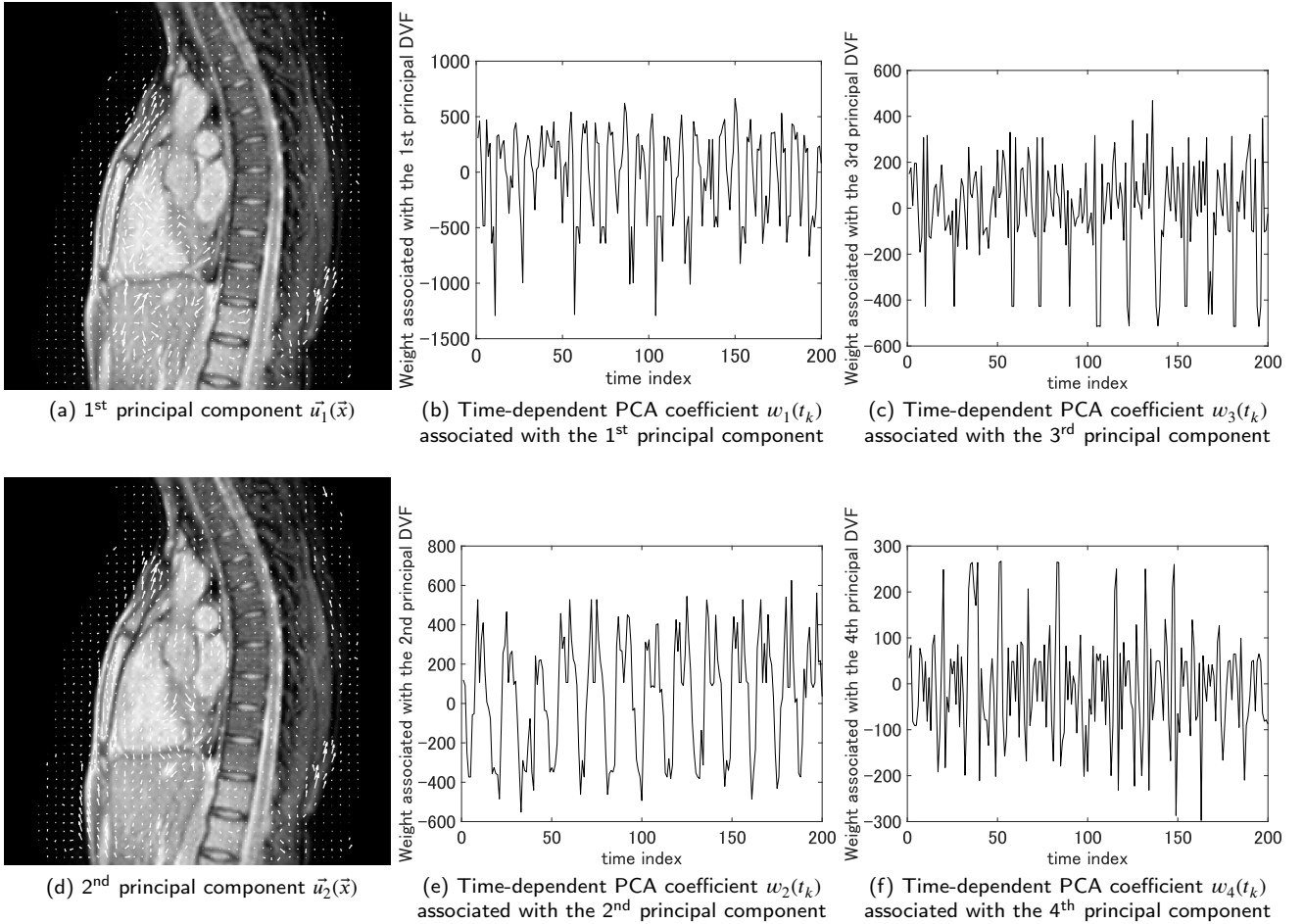


Figure 6: First two principal components and first four time-varying PCA coefficients associated with sequence 1. The first $M_{train} = 90$ images are used to compute the principal DVFs. The time-dependent weights are computed by projecting the DVF at time t onto the subspace spanned by the principal components (Eq. 3). The origins of each of the displayed 2D displacement vectors are separated from each other by 6 pixels (6mm). The principal DVFs were multiplied by a scalar coefficient equal to 500 to ease visualization. The image at $t = t_1$ is displayed in the background. Best viewed with zoom-in on a digital display.

ity in the loss gradient update in UORO and the additional random initialization of the coefficients A appearing in the synthetic gradient of DNI (same notation as in [23]).

3.2.1. Prediction performance

SnAp-1 and RTRL achieved the lowest weight prediction nRMSEs (averaged over the four sequences and horizon values examined), followed by DNI and then UORO (Table 3). In general, the nRMSE tended to increase with the horizon value (Fig. 8). Linear regression led to the lowest nRMSE at $h = 0.314s$, equal to 0.7866. RTRL and SnAp-1 outperformed the other algorithms when $h \geq 0.628s$, with associated nRMSEs lower than 0.8790. The error curves related to SnAp-1 and RTRL were quite close, indicating that the former algorithm approximated the latter well. Linear regression resulted in higher prediction errors than all RNN methods investigated when $h \geq 0.942s$, except when the hid-

⁷The confidence interval calculation method is the same as that described in Section 2.4 in [22].

den layer parameters were fixed. The latter method resulted in the worst accuracy for all values of h .

In Fig. 9, one can observe the synchronization of most peaks of $w_1(t)$ and $w_3(t)$ with the oscillations of $w_2(t)$, the main PCA weight associated with breathing motion in sequence 1. Predictions with SnAp-1 seem visually correct in general, although the peaks of the predicted signal do not perfectly match those of the original signal, especially for $w_3(t)$. That may lead to a lower breathing amplitude in the corresponding predicted 2D frames.

3.2.2. Influence of the hyper-parameters on prediction accuracy

Fig. 10 describes the influence of the hyper-parameters on the cross-validation nRMSE for UORO, SnAp-1, and DNI. The latter reveals that the forecasting error generally increased with h , which corroborates the observations regarding the test nRMSE in Fig. 8. These three RNN training algorithms attained the minimum of the nRMSE (averaged

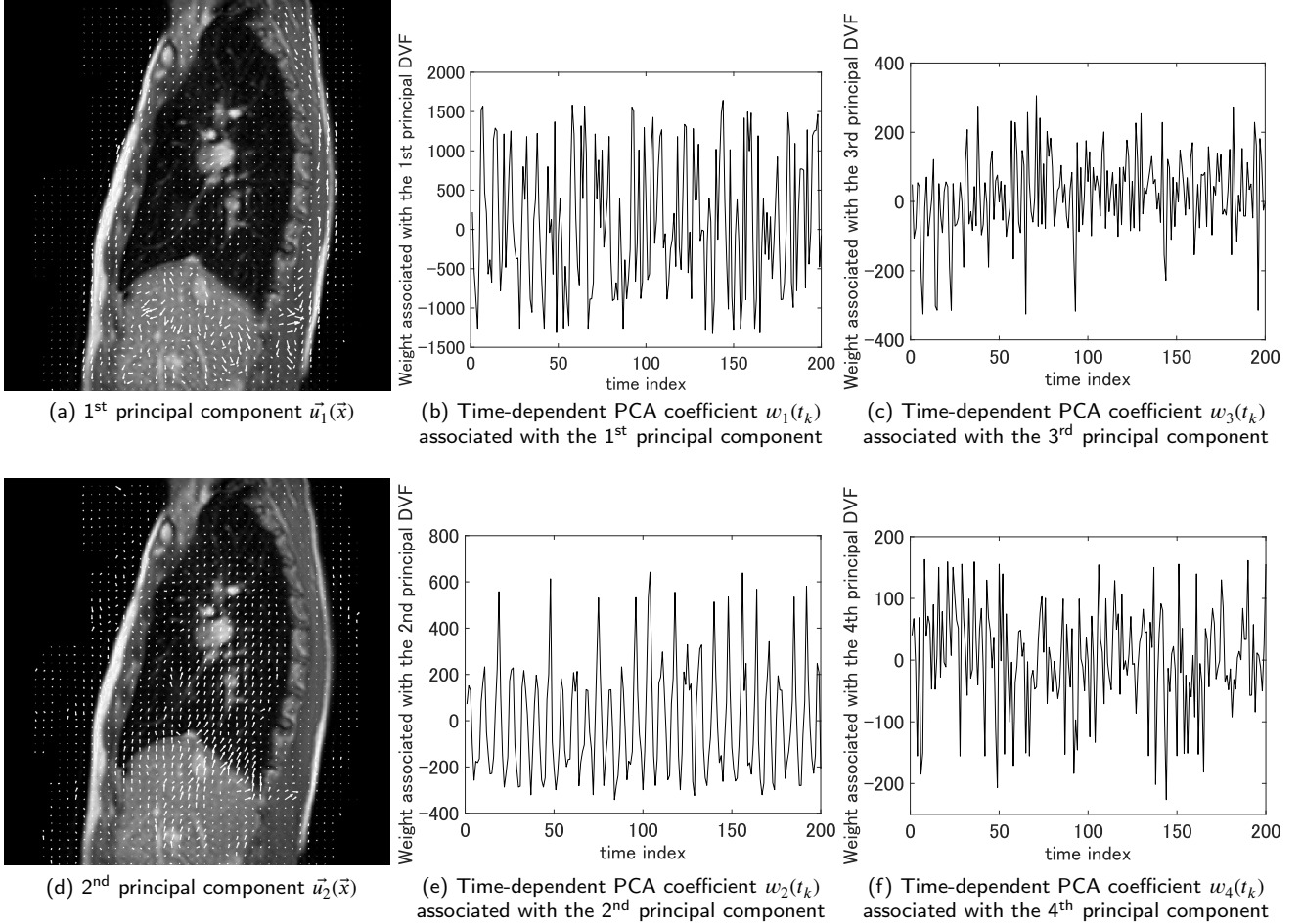


Figure 7: First two principal components and first four PCA coefficients associated with sequence 4 (for $M_{train} = 90$). The origins of each of the displayed 2D displacement vectors are separated from each other by 6 pixels. The norm of each principal DVF was multiplied by a coefficient equal to 500 to ease visualization. The image at $t = t_1$ is displayed in the background. Best viewed with zoom-in on a digital display.

over the seven horizon values) at an SHL equal to $L = 12$ time steps (which corresponds to 3.768s ahead). Furthermore, the learning rate that minimized that nRMSE was 0.01 for both UORO and DNI and 0.02 for SnAp-1. Concerning the latter algorithm, the cross-validation nRMSE decreased both with the learning rate η and number of hidden units q , irrespective of the horizon value selected. Optimizing η for SnAp-1 led to the most significant average nRMSE decrease (a 5.2% relative decrease), from 0.865 at $h = 0.314$ s to 0.793 at $h = 2.198$ s.

3.3. Optimization of the number of principal components

In this section and the following, the number of principal components n_{cp} is selected by cross-validation, as described in Section 2.4 (step 5 in Fig. 4). The registration error of the cross-validation set using the predicted DVF, $E_{pred}(n_{cp})$, defined in Eq. 10, tended to increase with the forecasting horizon h (Fig. 11), which coincides to the previous observations related to Figs. 8 and 10. Selecting only one component led to a high registration error, as the prin-

cipal component mainly associated with breathing was that of order 2 in three of the MR sequences (Section 3.1). The variation of $E_{pred}(n_{cp})$ with n_{cp} when $n_{cp} \geq 2$ was relatively low compared to the sharp error decline observed when n_{cp} increased from 1 to 2. When considering $E_{pred}(n_{cp})$ averaged over $h \in \{0.314\text{s}, \dots, 2.198\text{s}\}$ (black dotted curves in Fig. 11), it appears that selecting $n_{cp} = 2$ components was optimal for LMS, whose corresponding registration error increased significantly, from 0.2278 to 0.2313, as n_{cp} increased from 2 to 4. By contrast, $n_{cp} = 3$ minimized $E_{pred}(n_{cp})$ averaged over h for UORO, SnAp-1, RTRL, and linear regression, and $n_{cp} = 4$ was optimal for DNI.

Predictions at low response time intervals were generally more accurate using more principal components. Indeed, UORO and DNI attained their lowest registration error $E_{pred}(n_{cp})$ at $n_{cp} = 2$ when $h \geq 1.884$ s and $n_{cp} = 4$ when $h \leq 1.256$ s, respectively. Concerning LMS and linear regression, using three components was optimal for $h \leq 0.628$ s, and the predicted DVF was more accurate with $n_{cp} = 2$ when $h \geq 0.942$ s⁸. That phenomenon happened as the signals associated with higher-order principal com-

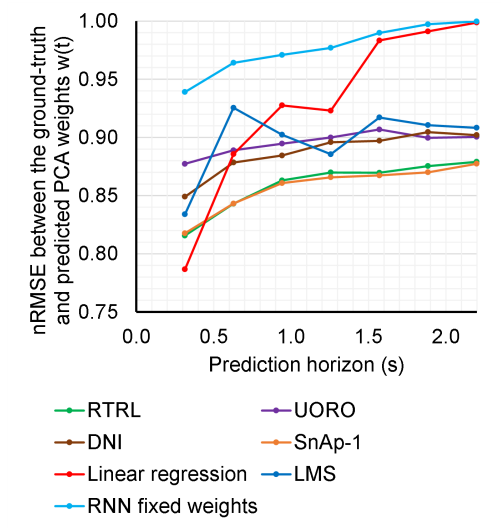


Figure 8: nRMSE of the test set associated with the prediction of the first three time-dependent PCA weights (Eq. 7 with $k_{min} = M_{cv} + 1$, $k_{max} = 200$, and $n_{cp} = 3$) for each algorithm as a function of the look-ahead time h . Each point represents the nRMSE averaged over the four sequences and $n_{test}^{PCA} = 250$ runs in the case of RNNs (except RTRL, for which we set $n_{test}^{PCA} = 10$ given its higher processing time and lower error uncertainty) for a given value of h . The hyper-parameters are selected by cross-validation as described in Section 2.3.

Prediction method	nRMSE
RTRL	0.8594 ± 0.0006
UORO	0.8954 ± 0.0006
SnAp-1	0.8574 ± 0.0001
DNI	0.8874 ± 0.0008
LMS	0.8976
Linear regression	0.9280
Previous weight as prediction	1.4580
RNN with frozen layer	0.9768 ± 0.0005

Table 3

nRMSE of the test set associated with the prediction of the first three time-dependent PCA weights (Eq. 7) for each algorithm, averaged over look-ahead time intervals between 0.32s and 2.20s, the four image sequences, and $n_{test}^{PCA} = 250$ runs in the case of RNNs (except RTRL, for which we set $n_{test}^{PCA} = 10$ given its higher processing time and precision). Each error value in the table corresponds to the average of one curve in Fig. 8. We assume that the nRMSEs associated with the RNNs follow each a Gaussian distribution and report the corresponding 95% confidence half-range intervals⁷.

ponents tended to be noisier and harder to forecast (Section 3.1). At low look-ahead time periods, they can be predicted to some extent, which leads to a more accurate DVF estimation, as these components still contain valuable information about chest motion. At higher horizons, though, reliable prediction becomes more challenging; therefore, discarding them can be a better choice. In other words, the information added by increasingly noisier weights was only worth considering if they could be predicted with a relatively high degree of confidence, which was more often the case when

h was low.

3.4. Image prediction

3.4.1. Numerical accuracy

To take into account the randomness involved in the initialization and updates of the synaptic weights, we report the image prediction performance metrics associated with the RNNs averaged over $n_{warp} = 25$ runs (except RTRL, for which $n_{warp} = 5$ due to its higher processing time and precision). LMS attained the highest cross-correlation coefficient and structural similarity index measure (SSIM), averaged over the four sequences and horizon values considered, between the predicted and original images [55], followed by SnAp-1 and RTRL (Table 4). Nonetheless, the average SSIM achieved by LMS, equal to 0.8991, was within the confidence interval of that associated with SnAp-1. By contrast, RTRL and SnAp-1 reached nRMSEs between the predicted and ground-truth test images, respectively equal to 0.2113 and 0.2115, lower than that corresponding to LMS, equal to 0.2135. It should be noted that the nRMSE referred to in Table 4 (and more generally in this section) differs from that in Table 3 and Fig. 8. Indeed, in the former, it characterizes the dissimilarity between the predicted and original images directly¹¹, as opposed to that between the predicted and ground-truth PCA weights, in the latter. SnAp-1 attained the lowest mean and maximum Euclidean endpoint errors (also referred to as geometrical errors) between the predicted and reference DVFs, respectively equal to 1.41mm and 21.28mm, where the ground-truth DVFs refer to the pyramidal Lucas-Kanade optical flow (Section 3.1). Indeed, the displacements derived from the latter method can still represent a valid benchmark, although the exact motion is not precisely known. The four RNN online training algorithms examined achieved a higher DVF prediction accuracy than LMS, whose corresponding mean and maximum deformation errors were equal to 1.48mm and 22.00mm, respectively.

Keeping the hidden layer of an untrained vanilla RNN unchanged as an edge case led to lower numerical accuracy measures than those corresponding to RNNs trained dynamically. Similarly, using the previous time-varying weights $w_j(t_k)$ or frame at time t_k as the predicted weights $w_j(t_{k+h-1})$ or frame at time t_{k+h-1} , respectively, as edge cases, resulted in a performance worse than that of the other forecasting algorithms investigated. Interestingly, the former scenario (using the past weights as the predicted ones)

⁸Selecting $n_{cp} = 3$ components was optimal for linear regression when $h = 2.198$ s. However, the values of $E_{pred}(n_{cp})$ for $n_{cp} = 2$ and $n_{cp} = 3$ were very close, which might be due to the relatively low number of sequences in our dataset. The curves corresponding to the intermediary horizon values $h = 0.628$ s, $h = 1.256$ s, and $h = 1.884$ s were not represented in Fig. 11 (and also Fig. 10) to improve readability.

⁹Same as footnote 7.

¹⁰That last row can be interpreted as an upper bound on the forecasting performance, intrinsic to the image registration method employed.

¹¹The nRMSE between the ground-truth and predicted images can be defined using the same formula as Eq. 7 by replacing the predicted weights $w_j^{pred}(t_k)$, the ground-truth weights $w_j^{true}(t_k)$, and the number of principal components n_{cp} by the predicted and ground-truth image intensity at pixel j and the number of pixels $|I|$, respectively.

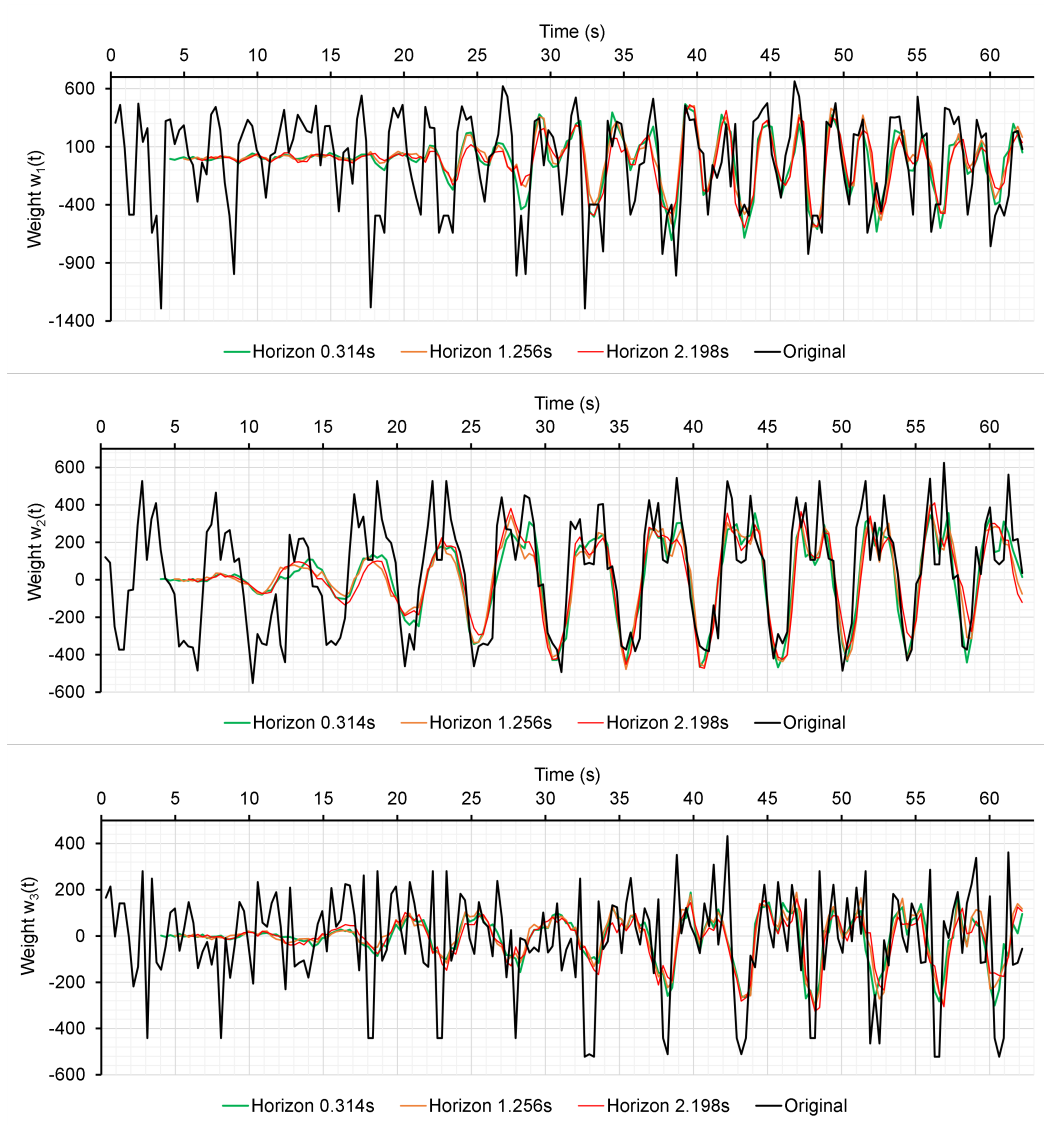


Figure 9: Prediction of the time-dependent PCA weights associated with sequence 1 for different horizon values using *SnAp-1*. The hyper-parameters are selected by cross-validation for each horizon value, as described in Section 2.3.

resulted in a better accuracy than the latter. That seems to confirm that discarding the higher-order PCA components had a regularizing effect relative to the initial deformation field and thus helped minimize noise in the predicted motion. Lastly, the similarity between the original image at time t_k and the first image (at time t_1) warped with the non-predicted DVF between t_1 and t_k , measured in terms of average cross-correlation, SSIM, and nRMSE, was higher than that of any of the forecasting techniques examined. That suggests that further enhancing PCA weight forecasting performance would likely lead to a higher video prediction accuracy.

The cross-correlation coefficient and SSIM between the predicted and ground-truth frames tended to decrease as h increased, irrespective of the algorithm considered (Fig. 12).

¹²Same as footnote 7.

Similarly, the nRMSE between the predicted and ground-truth frames and both the mean error and maximum error between the predicted and original DVF (computed using the Lucas-Kanade optical flow technique) tended to increase with h for all the forecasting approaches considered.

Linear regression was highly effective at $h = 0.314s$, as the associated nRMSE, mean DVF error, and maximum DVF error, equal to 0.2003, 1.297mm, and 20.24mm, respectively, were lower than those of the other methods. Moreover, linear regression achieved the lowest maximum DVF error at $h = 0.628s$, equal to 20.88mm. The cross-correlation and SSIM attained by LMS were the lowest among the algorithms compared when $h \leq 1.884s$ and $h \leq 1.570s$, respectively. Specifically, they decreased from 0.9888 to 0.9865 between $h = 0.314s$ and $h = 1.884s$ and from 0.9037 to 0.8979 between $h = 0.314s$ and $h = 1.570s$, respectively. Nevertheless, the cross-correlation associated

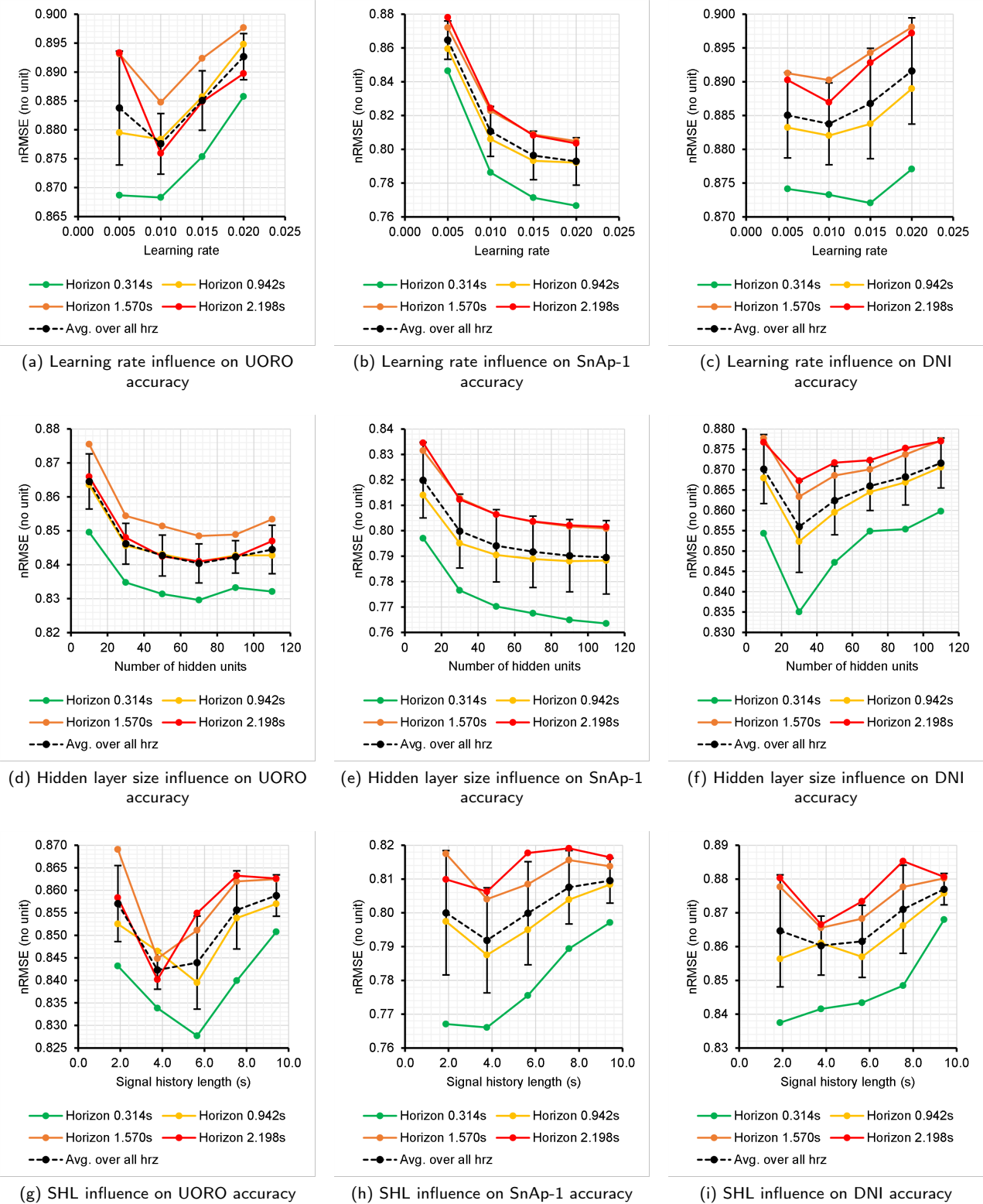


Figure 10: nRMSE between the predicted and ground-truth first three time-dependent PCA weights of the cross-validation set (Eq. 7 with $k_{min} = M_{train} + 1$, $k_{max} = M_{cv}$, and $n_{cp} = 3$). For a given hyper-parameter and specific value of h , each colored point in the corresponding graph represents the nRMSE minimum across all combinations of the other hyper-parameters within the cross-validation range (Table 2). Each nRMSE value displayed is averaged over $n_{cv} = 250$ runs and the four records. The black dotted curves and corresponding error bars represent the nRMSE minimum averaged over look-ahead times h between 0.314s and 2.198s and its standard deviation over these values of h , respectively.

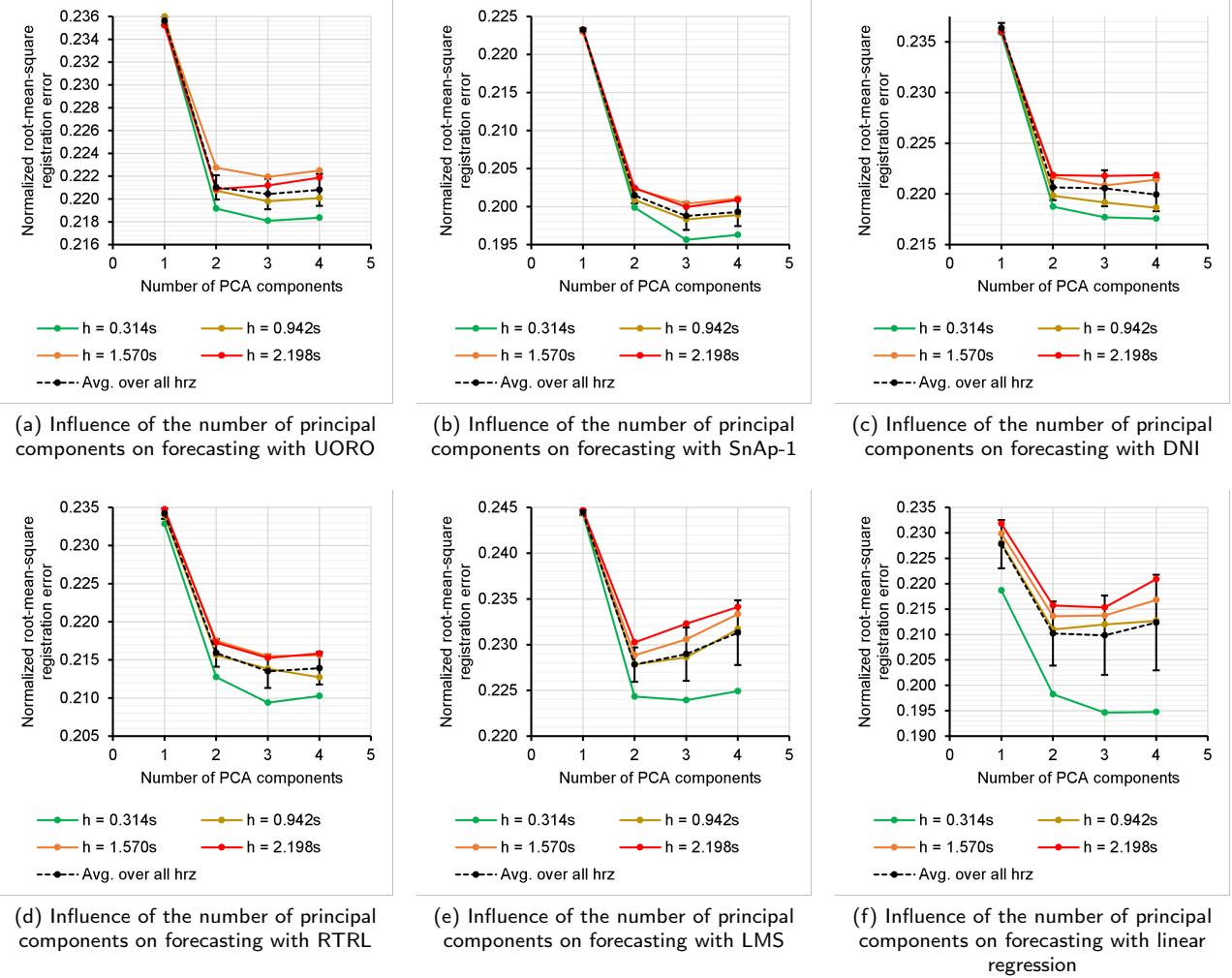


Figure 11: Normalized root-mean-square registration error $E_{pred}(n_{cp})$ using the predicted DVF of the cross-validation set (Eq. 10) as a function of the number of principal components n_{cp} for different forecasting algorithms and horizon values h . Each color point corresponds to the error average over the four sequences and $n_{warp} = 25$ runs in the case of RNNs (we set $n_{warp} = 5$ for RTRL as a specific case) for a given horizon value h . The RNN hyper-parameters were optimized by grid search for each value of n_{cp} and h . The black dashed curves and associated error bars correspond respectively to the average and standard deviation of $E_{pred}(n_{cp})$ over all the values of h between 0.314s and 2.198s.

with LMS was within the confidence interval of that of RTRL at $h = 1.884s$. Likewise, the SSIM corresponding to LMS was within the error range of the SSIMs of both RTRL and SnAp-1 at $h = 1.570s$. At $h = 2.198s$, all the RNN algorithms led to a predicted image cross-correlation with the ground truth higher than that of LMS, except DNI, whose associated confidence range overlapped that latter value nonetheless. The highest cross-correlation at $h = 2.198s$, equal to 0.9864, was attained by UORO. Similarly, the highest SSIMs for $h = 1.884s$ and $h = 2.198s$, respectively equal to 0.8979 and 0.8971, were achieved by SnAp-1. For those two highest look-ahead time periods, RNNs resulted in higher SSIMs than LMS, except UORO and DNI, whose confidence intervals nonetheless overlapped LMS. The lowest nRMSEs were attained by either RTRL or SnAp-1 for each horizon $h \in \{0.628s, \dots, 2.198s\}$, with an in-

crease from 0.2097 to 0.2144 for SnAp-1 between that interval's extremities. The nRMSEs associated with UORO and RTRL for h between 1.570s and 2.198s were also very close. Likewise, RTRL or SnAp-1 consistently achieved the lowest mean DVF error when $h \geq 0.628s$ and maximum DVF error when $h \geq 0.942s$. Concerning SnAp-1, these two geometrical errors respectively increased from 1.374mm to 1.440mm between $h = 0.628s$ and $h = 2.198s$ and from 21.16mm to 21.49mm between $h = 0.942s$ and $h = 2.198s$. RNNs systematically led to DVF errors lower than those corresponding to LMS when $h \geq 0.628s$, except for the maximum error attained by DNI at $h = 1.884s$, whose confidence range still comprised the maximum error of DNI for that specific horizon. There was a higher dispersion of the performance metrics corresponding to UORO and DNI around their mean (cf Table 4 also), similar to what was observed in Section 3.2

Prediction method	Cross-correlation coefficient	nRMSE	SSIM	Mean DVF error (mm)	Max DVF error (mm)
UORO	0.9863 ± 0.0001	0.2144 ± 0.0003	0.8971 ± 0.0002	1.450 ± 0.003	21.78 ± 0.03
SnAp-1	0.9868 ± 0.0001	0.2115 ± 0.0001	0.8990 ± 0.0001	1.405 ± 0.001	21.28 ± 0.01
DNI	0.9863 ± 0.0001	0.2151 ± 0.0005	0.8976 ± 0.0003	1.461 ± 0.005	21.68 ± 0.04
RTRL	0.9868 ± 0.0001	0.2113 ± 0.0001	0.8989 ± 0.0001	1.405 ± 0.001	21.31 ± 0.01
LMS	0.9872	0.2135	0.8991	1.479	22.00
Linear regression	0.9854	0.2176	0.8943	1.471	21.73
RNN with fixed hidden weights	0.9818 ± 0.0001	0.2335 ± 0.0002	0.8869 ± 0.0001	1.607 ± 0.002	23.25 ± 0.03
Previous PCA weight as prediction	0.9715	0.2755	0.8602	2.129	27.90
Previous image as prediction	0.9654	0.3176	0.8483	n/a	n/a
Warping with the original DVF	0.9909	0.1592	0.9179	n/a	n/a

Table 4

Comparison of the video prediction performance of each algorithm. Each value represents the average of a specific performance measure of the test set over the four image sequences, the look-ahead values h between 0.314s and 2.198s, and $n_{warp} = 25$ evaluation runs in the case of RNNs (except RTRL, for which $n_{warp} = 5$ given its higher processing time and precision). We assume that each performance metric associated with the RNNs follows a Gaussian distribution and report the corresponding 95% confidence half-range intervals⁹. The rows “previous image as prediction” and “previous PCA weight as prediction” correspond to the situations where the frame at time t_k and the time-dependent weights $w_j(t_k)$ are used as the predicted frame at time t_{k+h} and predicted PCA weights $w_j^{pred}(t_{k+h})$, respectively. The row “warping with the original DVF” corresponds to the mean difference between the images at time t_k and the original image at t_1 warped by the Lucas-Kanade optical flow between t_1 and t_k ¹⁰.

regarding weight forecasting.

3.4.2. Visual results

In the predicted images, the deformations of the organs and the up and down diaphragm motion due to breathing generally seem correct. However, the diaphragm position at the end-of-inhale phase appears slightly higher than expected in the predicted frames corresponding to sequence 1 (Fig. 13). That might be caused by inaccuracies in the prediction of the peaks of the time-dependent weights, as the sequences are relatively short (cf Fig. 9, especially the third-order signal). High intensity errors localized at the top of the right ventricle characterized the predicted frames at the end-of-exhale phase at $t = 59.0$ s in sequence 1, while the deformation errors, lower than 12mm, were rather homogeneous within the right ventricle and pancreas. At the end-of-inhale phase, both types of errors were higher, particularly within the small lung region posterior to the heart.

The intensity error mean of the test set in sequence 1 was pronounced around the latter air pocket and the diaphragm and heart boundaries (Fig. 14). In contrast, the deformation errors averaged over the test set were more diffuse across the organs, which was also the case in the other sequences. The moderate to high intensity errors located at the major vessels in sequences 2 and 4 did not correlate with significant geometrical errors in the same regions. In contrast to the other sequences, the intensity errors associated with liver motion in sequence 2 were localized at the diaphragm. Indeed, in the latter acquisition, the up and down liver movements were fast relative to the sampling frequency, as evidenced by the blurriness at the diaphragm area in the mean image. The corresponding deformation errors were concentrated near the posterior part of the liver, where the mean image appeared the least sharp and the motion amplitude was the highest. The displacements of organs such as the liver

and heart were accompanied by noise and temporal changes in local texture, which resulted in low and homogeneous intensity errors. Lastly, all sequences were characterized by relatively high errors at specific areas comprising the sternum, lumbar, and skin (or subcutaneous fat), partly due to high tissue/bone contrast and out-of-plane motion.

4. Discussion

4.1. Comparison with the literature about spatiotemporal respiratory motion forecasting

Table 5 compares our PCA-based model with the literature regarding next-frame prediction in 2D dynamic chest imaging. Comparison is complex because the datasets are different. In particular, the imaging modality, the exact human body part imaged, the spatial resolution, brightness, contrast, sampling frequency, and noise, as well as the frequency, amplitude, and regularity of the respiratory motion, vary from study to study. Furthermore, the experimental setting, which involves arbitrary choices regarding the response time and the data partition into development and test sets, also differs between the studies.

Chhatkuli et al. reported higher cross-correlations and SSIMs than those corresponding to our research [56]. However, they used repeated sequences, which made the input breathing data artificially regular and easy to predict. Moreover, our mathematical model, based on the computation of deformation fields, may better represent motion data than PCA applied directly to raw intensities, as it was reported that a large number of principal components (twenty) were used to predict the kV fluoroscopic images in that work.

¹³The hyper-parameters and value of n_{cp} that minimized the prediction RMSE between the original and predicted weights and the registration error of the cross-validation set, respectively, were selected for each sequence individually.

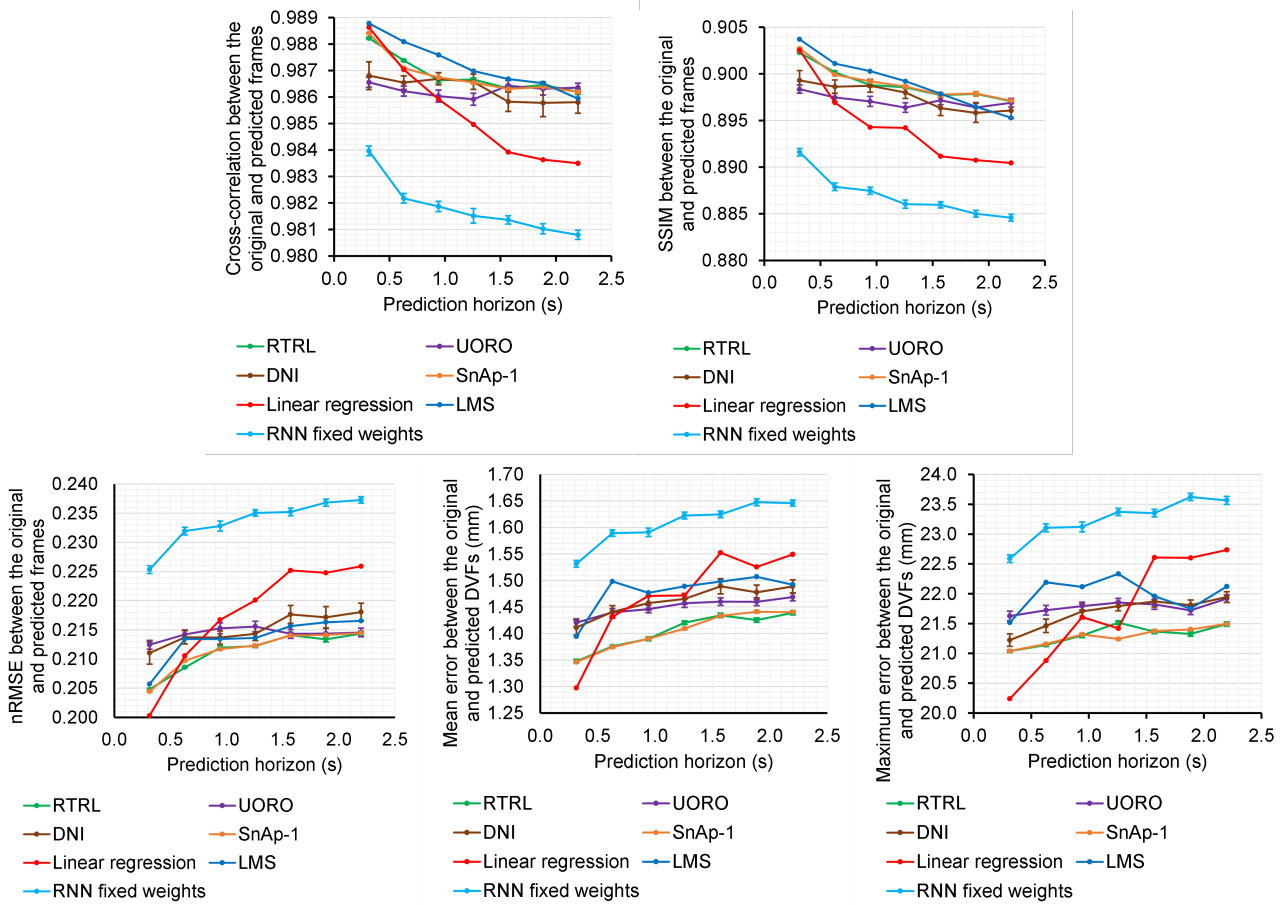


Figure 12: Future frame forecasting accuracy/errors corresponding to each algorithm as a function of the look-ahead time interval. Each point represents the average of a given performance metric of the test set over the four image sequences and $n_{warp} = 25$ runs in the case of RNNs (we set $n_{warp} = 5$ for RTRL as a specific case). We plotted the 95% confidence interval associated with the mean of each RNN performance measure, assuming that the latter follows a Gaussian distribution¹².

We conjecture that artifacts and inconsistencies in the predicted frames may become more pronounced with models based on direct pixel synthesis, such as that in [45] as well, when relatively large unseen deformations occur or when experimenting with high response time intervals. Indeed, Oprea et al. mention that methods leveraging only raw pixel intensities "often lead to the regression-to-the-mean problem, visually represented as blurriness" [35]. 4DCT data was also used in [45] and [46], which report higher SSIMs and low target tracking errors, respectively. Although the latter error type, corresponding to the motion of a few points only, is different from the geometrical or endpoint errors (average motion error over a whole 2D cross-section) in our study, their comparison is still significant to some extent. Nonetheless, 4DCT scans only capture an average motion over several respiratory cycles. Hence, these two studies may lack relevance in a clinical context, where efficient tracking must take intra-fractional breathing variations into account. In addition, it is currently impossible to acquire 4DCT scans in real-time during radiotherapy treatment.

The geometrical errors associated with RNNs in our research are lower than the tumor center-of-mass tracking er-

ror reported in [43] despite the lower horizons considered in the latter study (up to $h = 625$ ms). That happened because RNNs are intrinsically better than standard MLPs at modeling time-series data. Even though lower landmark tracking errors, corresponding to blood vessel positions, were achieved in [46], the images selected in the latter study only covered the right hemidiaphragm as an attempt to avoid motion not directly related to breathing. Indeed, Romaguera et al. conducted another experiment using sagittal cross-sections comprising the left lower lobe of the liver and featuring composite motion, including cardiac beating; with that setting, the local normalized cross-correlation dropped to 0.85 at $h = 1.60$ s. Those conditions were closer to our study, as sequences 1 and 4 included cardiac motion. Moreover, since we did not crop the images to focus on specific region of interests (ROI) and considered instead the whole chest, motion data compression and forecasting in our work were more challenging.

Table 5 does not encompass the entire body of literature about spatio-temporal respiratory motion forecasting for concision. However, the results reported in the previous related works are generally consistent with ours. For

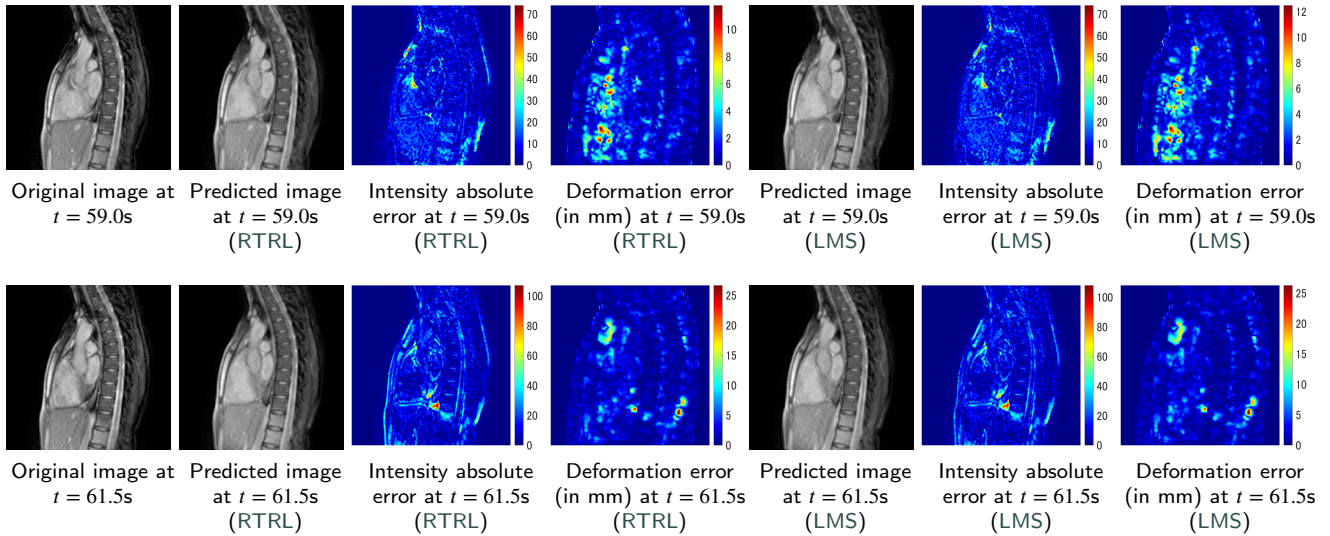


Figure 13: Predicted images in sequence 1 using RTRL at $h = 0.31s$ and LMS at $h = 1.88s$ at the end of expiration (top line, frame 188) and inspiration phases (bottom line, frame 196), along with the corresponding pixel-wise intensity and Euclidean deformation error maps. The predictions were performed with $n_{cp} = 3$ principal components, as that choice led to the best cross-validation accuracy for both methods. Among the algorithms compared, the highest SSIMs for sequence 1 with $h = 0.31s$ and $h = 1.88s$ were achieved by RTRL and LMS, respectively, with the hyper-parameters selected by cross-validation.

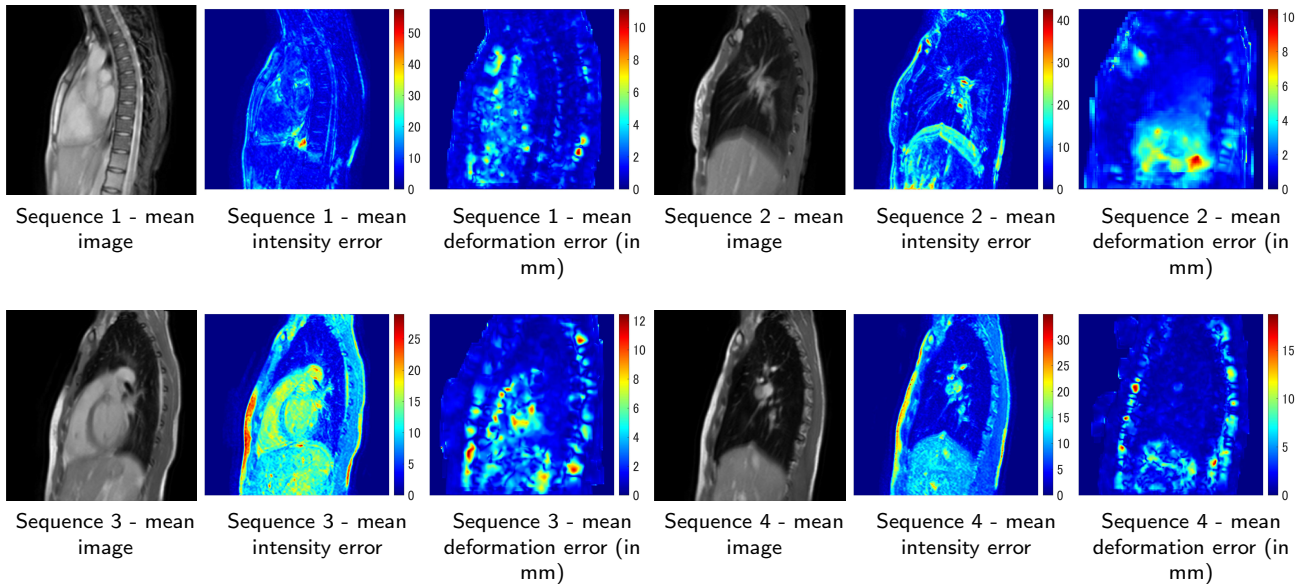


Figure 14: Spatial SnAp-1 prediction errors averaged over the test set and 5 evaluation runs with $h = 1.88s$, along with the mean image of the test set, for the four MRI sequences¹³.

instance, a 1.67mm geometric mean deformation error and SSIM of 0.75 were reported in [47], focusing on 4D-MR liver sequence reconstruction from a static 3D-MR volume and sagittal cine-MR navigator slices. The errors were likely higher due to the inherently more challenging task, which involved reconstructing a complete 4D sequence from partial observations in addition to time-series forecasting. Furthermore, the sequences used in that study seemed more diverse than ours regarding patient anatomies and breathing charac-

teristics (e.g., the authors mentioned irregularities such as small apneas). Most works mention that the forecasting accuracy tends to decrease as the prediction horizon increases. For instance, an increase of the tracking error relative to the tumor center of mass from 1.55mm to 2.6mm as h increased from 125ms to 625ms was reported for the XCAT phantom experiment in [43]. That study also mentioned a similar increase in the nRMSE relative to PCA time-dependent weight forecasting. Likewise, tumor SI positions extracted

Work	Prediction method	Type of video prediction model	Population or subject-specific?	Breathing data	Sampling rate	Amount of data	Response time	Prediction error
[56]	PCA and MSSA	Direct pixel synthesis	Subject-specific	1) kV fluoroscopy (phantom) 2) coronal cross-sections from lung cancer 4DCT	1) 10Hz 2) 2Hz	1 record of 24 (case 1) or 28 (case 2) repeated frames	1) 100ms 2) 500ms	1) c.c. 0.998 SSIM 0.971 2) c.c. 0.999 SSIM 0.995
[43]	PCA and MLP with adaptive boosting	Prediction space factorization with explicit transformations	Subject-specific	1) XCAT phantom 2) cine-MRI of liver cancer patient (both sagittal)	1) 8Hz 2) 3Hz	1) 5 records of 2 min 2) 1 min record	1) 125ms, 625ms 2) 333ms	1) 3D TE 1.55mm, 2.60mm 2) SI/AP TE 1.58mm/1.90mm
[45]	PredNet [30]	Direct pixel synthesis	Population	x/y/z cross-sections from 4DCT of lung cancer patients [57]	-	6 patients 10 phases per 2D sequence	-	SSIM from 0.935 to 0.951
[46]	Voxelmorph-like recurrent AE and spatial transformer	Prediction space factorization with explicit transformations	Population	1) liver sagittal cine-MRI from healthy subjects 2) chest sagittal cross-sections from 4DCT [58]	1) 3.13Hz 2) 2.5Hz	1) 12 records of 50 frames 2) 10 records of 10 frames	1) 0.32s to 1.60s 1) 0.40s to 2.0s	1) local c.c. 0.95-0.97 TE 0.45mm - 0.77mm 2) TE from 0.28mm to 0.42mm
Our work	PCA from Lucas-Kanade optical flow and SnAp-1	Prediction space factorization with explicit transformations	Subject-specific	Chest sagittal cine-MRI from healthy subjects	3.18Hz	4 records from 2 subjects with 200 frames per record	from 314ms to 2.198s	c.c. 0.987 SSIM 0.899 Mean geometrical DVF error 1.41mm

Table 5

Comparison of our work with the previous studies about next-frame forecasting in 2D chest imaging. A field with " - " indicates that the information is not available in the corresponding research article. "c.c." and "TE" respectively stand for "cross-correlation" and (target) "tracking error." The results corresponding to our study, in the last row, are those in Table 4; we selected SnAp-1 as a representative method for brevity. The column "type of video prediction model" refers to the classification in [35].

from cine-MR sequences (with a 4Hz sampling rate) were predicted in [16] using dynamically retrained LSTMs, and the corresponding RMSE increased with h , but with a wider spread, from 0.48mm at $h = 250$ ms to 2.20mm at $h = 750$ ms. However, it was reported in [59] that linear regression performed better than RNNs, as the former achieved a 1.65mm mean average 3D lung tumor tracking error at $h = 0.6$ s, using dynamic MR sequences sampled at 5Hz. That might be due to the relatively low values of h considered in that study. We conjecture that RNNs with online learning capabilities, such as those presented in our work, may perform better at higher horizons. More generally, it has commonly been observed that the prediction error increased with h in the broader literature about video forecasting. For instance, the graphs in [37, 36, 40] documenting a decreasing trend of the SSIM between the estimated and ground-truth frames as h increases were very similar to that in Fig. 12.

Deep learning-based population models such as those in [45, 46] enable inference on unseen patients without a prior additional registration step, but Romaguera et al. admit that "classical registration approaches still outperform deep learning techniques in several medical imaging applications" [46]. The end-to-end strategy in those studies contrasts with the modular pipeline that we adopted, similar to [56, 43]. The latter allows for better interpretability of the results, as the role of each PCA component and weight and their interaction can be examined simply (Section 3.1). Notably, while Nabavi et al. and Romaguera et al. focused mainly on the spatial modeling part using modern deep learning architectures,

we adopted a complementary approach by investigating for the first time recent online learning algorithms for RNNs, motivated by the need to adapt to non-stationary respiratory signals with few data (as large medical databases can be difficult to access), with an emphasis on the time-series forecasting component.

Moreover, our study is the first to tackle the optimal selection of the number of components n_{cp} in the PCA respiratory motion model in the context of chest MR scan sequence forecasting. Our results agree with the claim in [60] that two principal components are required to model the respiratory motion accurately. That argument was based on the fact that two eigenvectors are sufficient to represent cosine motion, which can approximate breathing to some extent. Similarly, the Bayesian information criterion was used in [9] to determine the optimal number of components experimentally; it was also found that the first two sufficed to describe motion in chest 4D-MRI. Likewise, it was mentioned in [43] that the third component appears "less predictable" than the first two. While we also visually observed that the noise level increased with the principal component index, we argue that cues helping better forecast motion are present in higher-order time-dependent weights and eigenvectors. Indeed, respiratory deformations cannot be fully reduced to a unidirectional cosine constituent. Our study is the first to propose a rationale based on self-supervised learning to optimize n_{cp} . The sharp drop in the registration errors as n_{cp} increases from 1 to 2 in Fig. 11 is consistent with the argument of the similarity of breathing motion with the cosine function mentioned in [60], while the general smaller de-

crease of $E_{pred}(n_{cp})$ as n_{cp} increases from 2 to 3 suggests that it is more complex than cosine motion. The prior studies about respiratory motion modeling with PCA generally used two or three principal components (Section 1.1); we also found in our work that that choice generally led to high forecasting accuracy. Specifically, we observed that the optimal value of n_{cp} depended on the prediction method, the horizon selected, and the image sequence itself. That aligns with the recommendation in [60] to determine the number of PCA coefficients on a patient-per-patient basis. Furthermore, the time-dependent weights $w_j(t)$ obtained from PCA in our study (Figs. 6 and 7) were visually similar to the PCA signals in [56, 43, 44], with the component mainly associated with breathing appearing rather sinusoidal and smooth.

4.2. Comments on the performance of RNNs

The prediction of the PCA weights $w_j(t)$ in this research is a task similar to that of the positions of external markers at 3.33Hz in [23], as the sampling frequency and data partition into training, cross-validation, and test sets (30s/30s/rest of the data, in the latter work) were similar. If we exclude RTRL, which was trained with fewer hidden units ($q \leq 40$) in [23], the algorithm ranking from lowest to highest nRMSE stayed the same (Table 3). Specifically, SnAp-1 achieved the lowest nRMSEs, followed in order by DNI, UORO, LMS, and linear regression, with reported error values in [23] (averaged over the horizon range considered, from $h = 0.3s$ to $h = 2.1s$) respectively equal to 0.335, 0.337, and 0.384, 0.490 and 1.663. However, the latter errors were lower than those corresponding to this work. Indeed, the PCA signals appeared noisier and more uncorrelated compared to the markers' location data in [23]. Moreover, the RNNs had less data to learn from in this research, as the number of time steps was lower, particularly within the test set, with which algorithms trained online can continue to improve. Nonetheless, in both works, the nRMSE tended to decrease with h and linear regression was particularly accurate at $h = 1$ step ahead forecasts (Fig. 8), with a corresponding nRMSE of 0.342 in [23].

The results relative to hyper-parameter optimization in [23] aligned with those in this research. Indeed, the cross-validation nRMSE as a function of q attained its global minimum for UORO at similar values in both works ($q = 70$ in this study and $q = 60$ in [23]). Likewise, concerning SnAp-1, the same error tended to decrease first as q increased, attaining a minimum at $q = 110$ in the current work and $q = 120$ in [23]. Lastly, the optimal learning rate η , corresponding to the minimum of the cross-validation nRMSE averaged over h , was 0.01 for both UORO and DNI, whereas the same error metric decreased with η and attained its minimum at $\eta = 0.02$ for SnAp-1, both in the current study (Fig. 10) and in [23]. By contrast, it was recommended in several articles about respiratory motion forecasting using signals with a sampling rate close to 30Hz to select a value of η ranging from 0.001 to 0.005 [12, 14, 15]. A higher value led to better results in our simulations, possibly due to the higher signal variations at lower sampling rates and the rel-

atively low amount of time steps in the time-series data that we used. Indeed, it was previously observed that the optimal learning rate tended to decrease as the acquisition frequency increased [23].

In our work, the RNNs accurately predicted the time-dependent PCA signals (Table 3), the DVFs, as evidenced by the corresponding low endpoint errors, and the future frames in terms of nRMSE (Table 4), compared with LMS and linear regression. However, the cross-correlation and SSIM associated with LMS in Table 4, respectively equal to 0.9872 and 0.8991, were the highest among the algorithms compared. We conjecture that as LMS has limited capabilities in forecasting noisy signals, cross-validation retained only $n_{cp} = 2$ components, on average over the four sequences and horizon values considered (Fig. 11), instead of $n_{cp} = 3$ or 4 for the RNNs. Selecting fewer components suppresses the influence of minor deformation modes on the predicted displacements, as respiratory motion was primarily associated with the first two components (Figs. 6 and 7). That denoising effect could explain why the average endpoint errors were lower for LMS despite the latter's better performance on several pixel intensity-based metrics. Generally, quantifying performance with multiple metrics allows for more fine-grained performance analysis: cross-correlation might be more sensitive to local image contrast differences, and SSIM quantifies image resemblance in a way that is more congruent with the perceptual characteristics of the human visual system. However, commonly used image similarity-based metrics such as those are imperfect, as they "prefer blurry predictions nearly accommodating the exact ground-truth than sharper and plausible but imperfect generations" [35]. In tumor motion tracking in radiotherapy, measures explicitly assessing the predicted DVF accuracy seem more relevant, as they as they relate more directly to the geometrical problem formulation. Moreover, RNNs still achieved a higher SSIM and cross-correlation at high horizons compared to LMS (Fig. 12) because of the latter's rudimentary memory capacity. With the advancement of MR-guided radiotherapy systems and the increase of MR image acquisition rates in the future, the horizon-to-acquisition frequency ratio will increase, which will likely make RNNs a more attractive option, even for relatively low look-ahead time periods. Lastly, the sequences in our dataset comprise relatively few time steps and feature rather stable motion; we hypothesize that later studies using more irregular breathing data will help even better experimentally highlight the robustness and benefits of online learning algorithms for RNNs relative to adaptive linear filters.

4.3. Limits of our study

Our MRI dataset is relatively limited, as only two subjects were involved. As such, more anatomies are needed to validate our preliminary findings in the future. In addition, the relatively short duration of our records may have impeded RNNs in efficiently modeling and forecasting respiratory signals in our experiments; using MR sequences with a longer acquisition time interval and more frames

in later works will improve performance. We conjecture that if longer records were available, the peaks of the time-dependent weights, such as those of $w_2(t)$ and $w_3(t)$ associated with sequence 1 in Fig. 9, may have been better estimated, leading to better accuracy at the two extreme phases of the breathing cycle. The end-of-inhale phase was challenging to predict due to higher inter-cycle variability, as indicated for instance by the predicted and ground-truth diaphragm misalignment in sequence 1 (Fig. 13). In general, errors can be high around the diaphragm, where motion amplitudes are higher, as evidenced by the corresponding average intensity mismatch in sequence 2 and blur in the associated mean test image (Fig. 14). These two observations agree with the findings in the related literature (Section 1.3). Nonetheless, our dataset still has the highest number of frames per sequence among those in the previous works about 2D frame prediction in chest imaging, except for the XCAT phantom data in [43] (Section 4.1). Furthermore, to the best of our knowledge, our study is the first to use publicly available data for video prediction in the context of 2D dynamic MR chest imaging. Our code is also publicly available [61]; thus, our experiments are fully reproducible. Lastly, the consistency of our results with the previous findings in the respiratory motion forecasting literature, highlighted above, indicates that our results are reliable.

In a real-world clinical setting, the out-of-plane motion of the patient during treatment and local variations in brightness and contrast may hamper accurate real-time registration and prediction. Furthermore, considering that the future 2D images are merely a deformation of the initial 2D frame is a convenient but restrictive hypothesis, as organ motion is three-dimensional and brightness constancy of local tissue is not guaranteed. A straightforward solution could be to update the motion model and reference frame used for warping when errors become large. Alternatively, one could develop an approach combining deformation field computation "with pure synthesis layers to better predict pixels that cannot be copied from other video frames," as suggested in [38], in future work. Although the Lucas-Kanade optical flow is a classical algorithm that has been used successfully in chest imaging [62, 63, 64], it may result in noisy DVFs, as it does not involve any assumption regarding field smoothness. In addition, it cannot cope with contrast and brightness variations, as it exclusively relies on the brightness constancy assumption and is not guided by an internal representation of object (or tissue) structures, as in deep learning-based registration [65]. Consequently, employing more sophisticated registration techniques in subsequent works will help improve the overall prediction accuracy. Still, our study is the first to discuss the optimization of the pyramidal and iterative Lucas-Kanade algorithm hyper-parameters in the context of chest cine-MR imaging (Appendix A). Lastly, although using PCA to model respiratory motion is a simple approach that enhances the explainability of the image prediction pipeline, the hypothesis that the motion vectors lie on a linear subspace is not exactly true. More complex representations with tools such as kernel principal com-

ponent analysis (kPCA) or auto-encoders (AE) could help overcome that limitation and improve the forecasting performance. Despite the shortcomings previously mentioned, our method experimentally satisfies the general 2mm maximum tracking error requirement often mentioned in the literature (cf for instance [66]), as the mean DVF error achieved by the RNNs in our work was less than 1.49mm for all the horizons considered (Fig. 12).

5. Conclusion

This work represents the first application of RNNs trained with online learning algorithms to the estimation of future frames in dynamic chest MR scan sequences and more broadly, to video prediction, to the best of our knowledge. RNNs were used to forecast the low-dimensional projection of the DVF between the reference image and incoming image, computed using the Lucas-Kanade pyramidal optical flow algorithm, onto the hyperplane spanned by the PCA components. After recovering the tissue displacements in the future using the PCA motion model, the initial sagittal cross-section was warped to estimate the next frames. Dynamic learning of RNNs is suited to the prediction of respiratory motion, as it enables adaptation to non-stationary breathing patterns and can help quickly reach high accuracy from a limited amount of training data. The proposed algorithm is highly interpretable and can separate and forecast composite motion, including cardiac beating and liver local deformations, on top of the main breathing component. We achieved performance on par with the related literature [56, 43, 45, 46], with a mean geometrical deformation error of 1.41mm for SnAp-1, corresponding to an average over the horizon values h considered, of up to 2.20s. Moreover, among the works about future frame prediction in medical chest dynamic imaging, ours is the first to make use of publicly available cine-MR sequences, and is thus fully reproducible. Our research will help compensate the latency of MR-guided radiotherapy systems and, in turn, deliver less radiation to healthy tissue.

In general, the accuracy of SnAp-1 was higher than that of DNI and UORO, and very close to that of RTRL, which was much more computationally expensive. The predictions tended to become less accurate as h increased. Linear regression was very efficient at low horizons: at $h = 0.31s$, it attained a mean DVF error equal to 1.30mm, which was lower than that of the other methods. That geometric error became then the lowest for SnAp-1 (and RTRL) between $h = 0.62s$ and $h = 2.20s$; it increased from 1.37mm to 1.44mm between these two values. Similarly, the SSIM achieved by LMS decreased from 0.904 to 0.898 as h increased from 0.31s to 1.57s, and was the highest among the algorithms compared for those values of h . SnAp-1 reached the highest SSIMs when $h \geq 1.88s$, with corresponding values of less than 0.898. The high performance of linear regression, adaptive linear filters and ANNs for low, intermediate, and high horizon values, respectively, agrees with the general literature on respiratory motion forecasting [4].

The predicted images appeared visually correct, although misalignments of the diaphragm edge sometimes appeared at the end-of-inhale phase, characterized by higher motion variability, in line with what has been documented in the previous works about chest image sequence prediction.

To the best of our knowledge, our study is the first to provide insights regarding optimization of n_{cp} , the number of coefficients in the PCA respiratory motion model, in the context of future frame prediction. Indeed, in the previous studies using that model, n_{cp} was selected rather arbitrarily, whereas ours are grounded on cross-validation. The first-order or second-order component corresponded primarily to respiratory motion. We observed that the others, reflecting minor modes of deformation such as cardiac or liver motion, could still contribute to performance improvements, although the associated time-varying weights looked noisier. Specifically, we observed that on average over the horizons h considered, $n_{cp} = 2$ led to the highest cross-validation accuracy for LMS and $n_{cp} \geq 3$ was better for the other methods. The sharp error drop observed from $n_{cp} = 1$ to $n_{cp} = 2$ is consistent with the fact that the main component associated with breathing was the second in three of the four sequences. In addition, the predictions corresponding to a high look-ahead time period h were more accurate when n_{cp} was lower and vice-versa. Indeed, at high response times, it is more challenging to forecast higher-order noisy PCA signals, and the latter contain less information regarding respiratory motion.

Predicting chest dynamic MR scan images presented specific difficulties including the presence of artifacts, the relatively low image acquisition frequency, and out-of-plane motion. The sequences in our dataset had a limited duration, corresponding to 200 frames, which made prediction even more challenging. Indeed, the RNNs needed to quickly adapt to each respiratory record with few training examples, as our approach is subject-specific. However, to the best of our knowledge, our dataset comprises the highest number of frames per (non-phantom) subject among the studies about future frame forecasting in chest dynamic imaging [56, 43, 45, 46]. Our method demonstrated performance satisfying the general clinical requirement of a 2mm maximum tracking error [66], but future works need to assess robustness to irregular breathing and variability in patient anatomies more thoroughly. In addition, while 2D chest video prediction can provide useful information about the motion and deformation of the tumor, its clinical benefits can only be fully realized in conjunction with modules performing downstream tasks such as segmentation to provide the actual contours of the tumor and organs at risk, and 3D image generation from partial 2D views to compensate for the 4D imaging limitations of MR-LINAC systems. The implementation and evaluation of such components combined together with our video prediction model is left as future work.

Conflicts of interest statement

The authors declare no conflict of interest.

Funding

This work was supported by the Epson International Scholarship Foundation and the Japan Student Services Organization.

Acknowledgments

We are thankful to Prof. Masaki Sekino, Prof. Ichiro Sakuma, Prof. Hitoshi Tabata (The University of Tokyo, Graduate School of Engineering) and Dr. Kiwoo Lee (Edogawa Hospital, Department of Radiology) for their thoughtful feedback and recommendations that helped enhance the quality of this research. We also express gratitude to Dr. Cristian Le Minh (Max Planck Institute) and Mr. Suryanarayanan N.A.V. (The University of Tokyo, Graduate School of Engineering) for their assistance regarding software and coding.

Data and code availability

The data and code used in this research are publicly available online [49, 61].

References

- [1] E. Huynh, A. Hosny, C. Guthier, D. S. Bitterman, S. F. Petit, D. A. Haas-Kogan, B. Kann, H. J. Aerts, R. H. Mak, Artificial intelligence in radiation oncology, *Nature Reviews Clinical Oncology* 17 (2020) 771–781.
- [2] S. Sarudis, A. Karlsson Hauer, J. Nyman, A. Bäck, Systematic evaluation of lung tumor motion using four-dimensional computed tomography, *Acta Oncologica* 56 (2017) 525–530.
- [3] S. Takao, N. Miyamoto, T. Matsuura, R. Onimaru, N. Katoh, T. Inoue, K. L. Sutherland, R. Suzuki, H. Shirato, S. Shimizu, Intrafractional baseline shift or drift of lung tumor motion during gated radiation therapy with a real-time tumor-tracking system, *International Journal of Radiation Oncology - Biology - Physics* 94 (2016) 172–180.
- [4] P. Verma, H. Wu, M. Langer, I. Das, G. Sandison, Survey: real-time tumor motion prediction for image-guided radiation treatment, *Computing in Science & Engineering* 13 (2010) 24–35.
- [5] G. Wang, Z. Li, G. Li, G. Dai, Q. Xiao, L. Bai, Y. He, Y. Liu, S. Bai, Real-time liver tracking algorithm based on LSTM and SVR networks for use in surface-guided radiation therapy, *Radiation Oncology* 16 (2021) 1–12.
- [6] J. Ehrhardt, C. Lorenz, et al., 4D modeling and estimation of respiratory motion for radiation therapy, volume 10, Springer, 2013.
- [7] Q. Zhang, A. Pevsner, A. Hertanto, Y.-C. Hu, K. E. Rosenzweig, C. C. Ling, G. S. Mageras, A patient-specific respiratory model of anatomical motion for radiation treatment planning, *Medical physics* 34 (2007) 4772–4781.
- [8] H. Chen, Z. Zhong, Y. Yang, J. Chen, L. Zhou, X. Zhen, X. Gu, Internal motion estimation by internal-external motion modeling for lung cancer radiotherapy, *Scientific reports* 8 (2018) 1–14.
- [9] B. Stemkens, R. H. Tjissen, B. D. De Senneville, J. J. Lagendijk, C. A. Van Den Berg, Image-driven, model-based 3D abdominal motion estimation for MR-guided radiotherapy, *Physics in Medicine & Biology* 61 (2016) 5335.
- [10] W. Harris, L. Ren, J. Cai, Y. Zhang, Z. Chang, F.-F. Yin, A technique for generating volumetric cine-magnetic resonance imaging, *International Journal of Radiation Oncology - Biology - Physics* 95 (2016) 844–853.
- [11] L. V. Romaguera, T. Mezheritsky, R. Mansour, W. Tanguay, S. Kadoury, Predictive online 3D target tracking with population-based generative networks for image-guided radiotherapy, *International*

- tional Journal of Computer Assisted Radiology and Surgery 16 (2021) 1213–1225.
- [12] H. Lin, C. Shi, B. Wang, M. F. Chan, X. Tang, W. Ji, Towards real-time respiratory motion prediction based on long short-term memory neural networks, *Physics in Medicine & Biology* 64 (2019) 085010.
 - [13] R. Wang, X. Liang, X. Zhu, Y. Xie, A feasibility of respiration prediction based on deep bi-LSTM for real-time tumor tracking, *IEEE Access* 6 (2018) 51262–51268.
 - [14] S. Yu, J. Wang, J. Liu, R. Sun, S. Kuang, L. Sun, Rapid prediction of respiratory motion based on bidirectional gated recurrent unit network, *IEEE Access* 8 (2020) 49424–49435.
 - [15] P. Samadi Miandoab, S. Saramad, S. Setayeshi, Respiratory motion prediction based on deep artificial neural networks in CyberKnife system: A comparative study, *Journal of Applied Clinical Medical Physics* 24 (2023) e13854.
 - [16] E. Lombardo, M. Rabe, Y. Xiong, L. Nierer, D. Cusumano, L. Placidi, L. Boldrini, S. Corradini, M. Niyazi, C. Belka, et al., Offline and online LSTM networks for respiratory motion prediction in MR-guided radiotherapy, *Physics in Medicine & Biology* 67 (2022) 095006.
 - [17] H. Jaeger, Tutorial on training recurrent neural networks, covering BPPT, RTRL, EKF and the "echo state network" approach, volume 5, GMD-Forschungszentrum Informationstechnik Bonn, 2002.
 - [18] R. J. Williams, D. Zipser, A learning algorithm for continually running fully recurrent neural networks, *Neural computation* 1 (1989) 270–280.
 - [19] K. Jiang, F. Fujii, T. Shiinoki, Prediction of lung tumor motion using nonlinear autoregressive model with exogenous input, *Physics in Medicine & Biology* 64 (2019) 21NT02.
 - [20] M. Mafi, S. M. Moghadam, Real-time prediction of tumor motion using a dynamic neural network, *Medical & biological engineering & computing* 58 (2020) 529–539.
 - [21] M. Pohl, M. Uesaka, K. Demachi, R. B. Chhatkuli, Prediction of the motion of chest internal points using a recurrent neural network trained with real-time recurrent learning for latency compensation in lung cancer radiotherapy, *Computerized Medical Imaging and Graphics* (2021) 101941.
 - [22] M. Pohl, M. Uesaka, H. Takahashi, K. Demachi, R. B. Chhatkuli, Prediction of the position of external markers using a recurrent neural network trained with unbiased online recurrent optimization for safe lung cancer radiotherapy, *Computer Methods and Programs in Biomedicine* 222 (2022) 106908.
 - [23] M. Pohl, M. Uesaka, H. Takahashi, K. Demachi, R. B. Chhatkuli, Respiratory motion forecasting with online learning of recurrent neural networks for safety enhancement in externally guided radiotherapy, *arXiv preprint arXiv:2403.01607* (2024).
 - [24] O. Marschall, K. Cho, C. Savin, A unified framework of online learning algorithms for training recurrent neural networks, *Journal of Machine Learning Research* 21 (2020) 1–34.
 - [25] C. Tallec, Y. Ollivier, Unbiased online recurrent optimization, *arXiv preprint arXiv:1702.05043* (2017).
 - [26] J. Menick, E. Elsen, U. Evci, S. Osindero, K. Simonyan, A. Graves, A practical sparse approximation for real time recurrent learning, *arXiv preprint arXiv:2006.07232* (2020).
 - [27] S. Hochreiter, J. Schmidhuber, Long short-term memory, *Neural computation* 9 (1997) 1735–1780.
 - [28] M. Minderer, C. Sun, R. Villegas, F. Cole, K. P. Murphy, H. Lee, Unsupervised learning of object structure and dynamics from videos, *Advances in Neural Information Processing Systems* 32 (2019).
 - [29] X. Jin, H. Xiao, X. Shen, J. Yang, Z. Lin, Y. Chen, Z. Jie, J. Feng, S. Yan, Predicting scene parsing and motion dynamics in the future, *arXiv preprint arXiv:1711.03270* (2017).
 - [30] W. Lotter, G. Kreiman, D. Cox, Deep predictive coding networks for video prediction and unsupervised learning, 2017. *arXiv:1605.08104*.
 - [31] P. Luc, C. Couprie, Y. Lecun, J. Verbeek, Predicting future instance segmentation by forecasting convolutional features, in: *Proceedings of the European Conference on Computer Vision (ECCV)*, 2018, pp. 584–599.
 - [32] X. Shi, Z. Chen, H. Wang, D.-Y. Yeung, W.-K. Wong, W.-c. Woo, Convolutional LSTM network: A machine learning approach for precipitation nowcasting, *arXiv preprint arXiv:1506.04214* (2015).
 - [33] I. Sutskever, O. Vinyals, Q. V. Le, Sequence to sequence learning with neural networks, *Advances in neural information processing systems* 27 (2014).
 - [34] N. Srivastava, E. Mansimov, R. Salakhudinov, Unsupervised learning of video representations using LSTMs, in: *International conference on machine learning*, PMLR, 2015, pp. 843–852.
 - [35] S. Oprea, P. Martinez-Gonzalez, A. Garcia-Garcia, J. A. Castro-Vargas, S. Orts-Escolano, J. Garcia-Rodriguez, A. Argyros, A review on deep learning techniques for video prediction, *IEEE Transactions on Pattern Analysis and Machine Intelligence* (2020).
 - [36] R. Villegas, J. Yang, S. Hong, X. Lin, H. Lee, Decomposing motion and content for natural video sequence prediction, *arXiv preprint arXiv:1706.08033* (2017).
 - [37] C. Finn, I. Goodfellow, S. Levine, Unsupervised learning for physical interaction through video prediction, *arXiv preprint arXiv:1605.07157* (2016).
 - [38] Z. Liu, R. A. Yeh, X. Tang, Y. Liu, A. Agarwala, Video frame synthesis using deep voxel flow, in: *Proceedings of the IEEE International Conference on Computer Vision*, 2017, pp. 4463–4471.
 - [39] M. Jaderberg, K. Simonyan, A. Zisserman, K. Kavukcuoglu, Spatial transformer networks, *arXiv preprint arXiv:1506.02025* (2015).
 - [40] M. Babaeizadeh, C. Finn, D. Erhan, R. H. Campbell, S. Levine, Stochastic variational video prediction, *arXiv preprint arXiv:1710.11252* (2017).
 - [41] E. Denton, R. Fergus, Stochastic video generation with a learned prior, in: *International conference on machine learning*, PMLR, 2018, pp. 1174–1183.
 - [42] R. B. Chhatkuli, K. Demachi, N. Miyamoto, M. Uesaka, A. Haga, et al., Dynamic image prediction using principal component and multi-channel singular spectral analysis: a feasibility study, *Open Journal of Medical Imaging* 5 (2015) 133.
 - [43] J. Pham, W. Harris, W. Sun, Z. Yang, F.-F. Yin, L. Ren, Predicting real-time 3D deformation field maps (DFM) based on volumetric cine MRI (VC-MRI) and artificial neural networks for on-board 4D target tracking: a feasibility study, *Physics in Medicine & Biology* 64 (2019) 165016.
 - [44] W. Liu, A. Sawant, D. Ruan, Prediction of high-dimensional states subject to respiratory motion: a manifold learning approach, *Physics in Medicine & Biology* 61 (2016) 4989.
 - [45] S. Nabavi, M. Abdoos, M. E. Moghaddam, M. Mohammadi, Respiratory motion prediction using deep convolutional long short-term memory network, *Journal of Medical Signals and Sensors* 10 (2020) 69.
 - [46] L. V. Romaguera, R. Plantefève, F. P. Romero, F. Hébert, J.-F. Carrier, S. Kadoury, Prediction of in-plane organ deformation during free-breathing radiotherapy via discriminative spatial transformer networks, *Medical image analysis* 64 (2020) 101754.
 - [47] L. V. Romaguera, T. Mezheritsky, R. Mansour, J.-F. Carrier, S. Kadoury, Probabilistic 4D predictive model from in-room surrogates using conditional generative networks for image-guided radiotherapy, *Medical image analysis* 74 (2021) 102250.
 - [48] L. V. Romaguera, S. Alley, J.-F. Carrier, S. Kadoury, Conditional-based transformer network with learnable queries for 4D deformation forecasting and tracking, *IEEE Transactions on Medical Imaging* 42 (2023) 1603–1618.
 - [49] ETH Zürich, Biomedical Image Computing, Datasets, 4D MRI lung data, <https://bmic.ee.ethz.ch/research/datasets.html>, 2021. [Online; accessed 26-May-2021].
 - [50] M. von Siebenthal, G. Szekely, U. Gamper, P. Boesiger, A. Lomax, P. Cattin, 4D MR imaging of respiratory organ motion and its variability, *Physics in Medicine & Biology* 52 (2007) 1547.
 - [51] D. Boye, G. Samei, J. Schmidt, G. Székely, C. Tanner, Population based modeling of respiratory lung motion and prediction from partial information, in: *Medical Imaging 2013: Image Processing*, volume 8669, International Society for Optics and Photonics, 2013, p. 86690U.

- [52] B. D. Lucas, T. Kanade, et al., An iterative image registration technique with an application to stereo vision (1981).
- [53] J.-Y. Bouguet, et al., Pyramidal implementation of the affine Lucas Kanade feature tracker, description of the algorithm, Intel Corporation 5 (2001) 4.
- [54] R. Pascanu, T. Mikolov, Y. Bengio, On the difficulty of training recurrent neural networks, in: International conference on machine learning, 2013, pp. 1310–1318.
- [55] Z. Wang, A. C. Bovik, H. R. Sheikh, E. P. Simoncelli, Image quality assessment: from error visibility to structural similarity, IEEE transactions on image processing 13 (2004) 600–612.
- [56] Chhatkuli, Development of a markerless tumor prediction system using principal component analysis and multi-channel singular spectral analysis with real-time respiratory phase recognition in radiation therapy, Ph.D. thesis, The University of Tokyo, 2016. URL: https://repository.dl.itc.u-tokyo.ac.jp/record/48459/files/A32580_summary.pdf.
- [57] J. Vandemeulebroucke, D. Sarrut, P. Clarysse, et al., The POPI-model, a point-validated pixel-based breathing thorax model, in: XVth international conference on the use of computers in radiation therapy (ICCR), volume 2, 2007, pp. 195–199.
- [58] E. Castillo, R. Castillo, J. Martinez, M. Shenoy, T. Guerrero, Four-dimensional deformable image registration using trajectory modeling, Physics in Medicine & Biology 55 (2009) 305.
- [59] Y. Li, Z. Li, J. Zhu, B. Li, H. Shu, D. Ge, Online prediction for respiratory movement compensation: a patient-specific gating control for MRI-guided radiotherapy, Radiation Oncology 18 (2023) 149.
- [60] R. Li, J. H. Lewis, X. Jia, T. Zhao, W. Liu, S. Wuenschel, J. Lamb, D. Yang, D. A. Low, S. B. Jiang, On a PCA-based lung motion model, Physics in Medicine & Biology 56 (2011) 6009.
- [61] M. Pohl, pohl-michel/2d-mr-image-prediction: First release, 2024. URL: <https://doi.org/10.5281/zenodo.13896202>. doi:10.5281/zenodo.13896202.
- [62] Q. Xu, R. J. Hamilton, R. A. Schowengerdt, B. Alexander, S. B. Jiang, Lung tumor tracking in fluoroscopic video based on optical flow, Medical physics 35 (2008) 5351–5359.
- [63] Y. Akino, R.-J. Oh, N. Masai, H. Shiomi, T. Inoue, Evaluation of potential internal target volume of liver tumors using cine-MRI, Medical physics 41 (2014) 111704.
- [64] J. Dhont, J. Vandemeulebroucke, D. Cusumano, L. Boldrini, F. Cellini, V. Valentini, D. Verellen, Multi-object tracking in MRI-guided radiotherapy using the tracking-learning-detection framework, Radiotherapy and Oncology 138 (2019) 25–29.
- [65] G. Balakrishnan, A. Zhao, M. R. Sabuncu, J. Guttag, A. V. Dalca, Voxelmorph: a learning framework for deformable medical image registration, IEEE transactions on medical imaging 38 (2019) 1788–1800.
- [66] M. J. Murphy, Tracking moving organs in real time, in: Seminars in radiation oncology, volume 14, Elsevier, 2004, pp. 91–100.
- [67] D. Fleet, Y. Weiss, Optical flow estimation, in: Handbook of mathematical models in computer vision, Springer, 2006, pp. 237–257.
- [68] G. Zhang, T.-C. Huang, T. Guerrero, K.-P. Lin, C. Stevens, G. Starkschall, K. Forster, Use of three-dimensional (3D) optical flow method in mapping 3D anatomic structure and tumor contours across four-dimensional computed tomography data, Journal of applied clinical medical physics 9 (2008) 59–69.

A. Appendix : Optimization of the image registration parameters

In this section, we provide details regarding optimization of the parameters of chest MR scan registration with the iterative and pyramidal Lucas-Kanade optical flow algorithm [52, 67, 53] (step 1 in Fig. 4). To determine those resulting in the most accurate DVF for each image sequence, we minimize the "ground-truth" registration error $E_{gt}(\vec{u})$ of the

Parameter	Parameter range	Best value(s)
Std deviation of the Gaussian filter applied to the initial image	$\sigma_{init}^{DVF} \in \{0.1, 0.5, 1.0\}$	0.1
Std. deviation of the Gaussian filter used for downsampling at each layer	$\sigma_{sub} \in \{0.1, 0.5, 1.0\}$	-
Std. deviation of the Gaussian kernel weighting the moment matrix	$\sigma_{LK} \in \{1.0, 2.0, 3.0, 4.0\}$	2.0 or 3.0
Number of layers	$n_{layers} \in \{1, 2, 3\}$	2 or 3
Number of iterations	$n_{iter} \in \{1, 2, 3\}$	1

Table 6

Hyper-parameter range for optimization of the pyramidal iterative Lucas-Kanade algorithm, along with parameter values that experimentally led to the lowest registration error E_{gt} with the $M_{train} = 90$ first images of the four MR image sequences¹⁶.

first $M_{train} = 90$ images¹⁴, defined in Eq. 11. In that equation, $|I|$ refers to the number of pixels in a given image and $\delta(\vec{u}, \vec{x}, t_k)$ to the instant registration error at pixel \vec{x} and time t_k using the 4D vector field \vec{u} (Eq. 8)¹⁵. The parameters to determine, whose exact definition can be found in [21], their corresponding range for grid search, and their optimal value, are outlined in Table 6.

$$E_{gt}(\vec{u}) = \sqrt{\frac{1}{(M_{train} - 1)|I|} \sum_{k=2}^{M_{train}} \sum_{\vec{x}} \delta(\vec{u}, \vec{x}, t_k)^2} \quad (11)$$

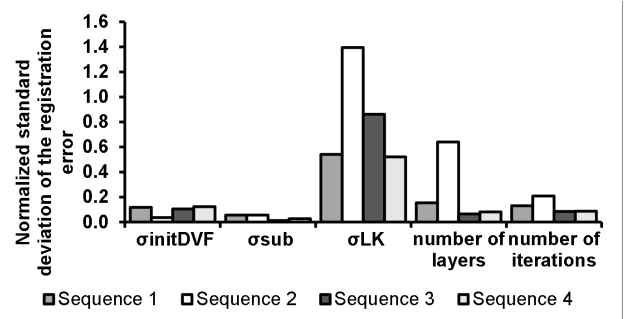


Figure 15: Relative influence of the iterative and pyramidal Lucas-Kanade optical flow algorithm parameters on the (minimum) registration error E_{gt} . Each bar corresponds to the standard deviation associated with one curve in Fig. 16.

E_{gt} increased with σ_{init}^{DVF} and σ_{sub} , except for sequence 2, where it decreased with σ_{sub} (Fig. 16). These observations, similar to those relative to chest CT scan registration in [21], indicate that initial filtering seems to have a detrimental effect on registration. E_{gt} was a convex function of

¹⁴Registration was also optimized using the first 90 images when forecasting the PCA weights with linear regression, although we selected $M_{train} = 160$ for that algorithm (Section 2.3).

¹⁵ E_{gt} refers to the same quantity as e_{DVF} in [21]. The deformation field \vec{u} minimizing $E_{gt}(\vec{u})$ in Eq. 11 is considered the "ground-truth" DVF, representing the motion to forecast. Therefore, the field \vec{u} intervening in the expression of E_{gt} does not depend on any evaluation run index i or number of principal components n_{cp} , as opposed to $\vec{u}^{(i)}(n_{cp})$, appearing in the definition of the registration error $E_{pred}(n_{cp})$ (Eq. 10) and corresponding to the predicted DVF.

¹⁶The notations are the same as those in [21].

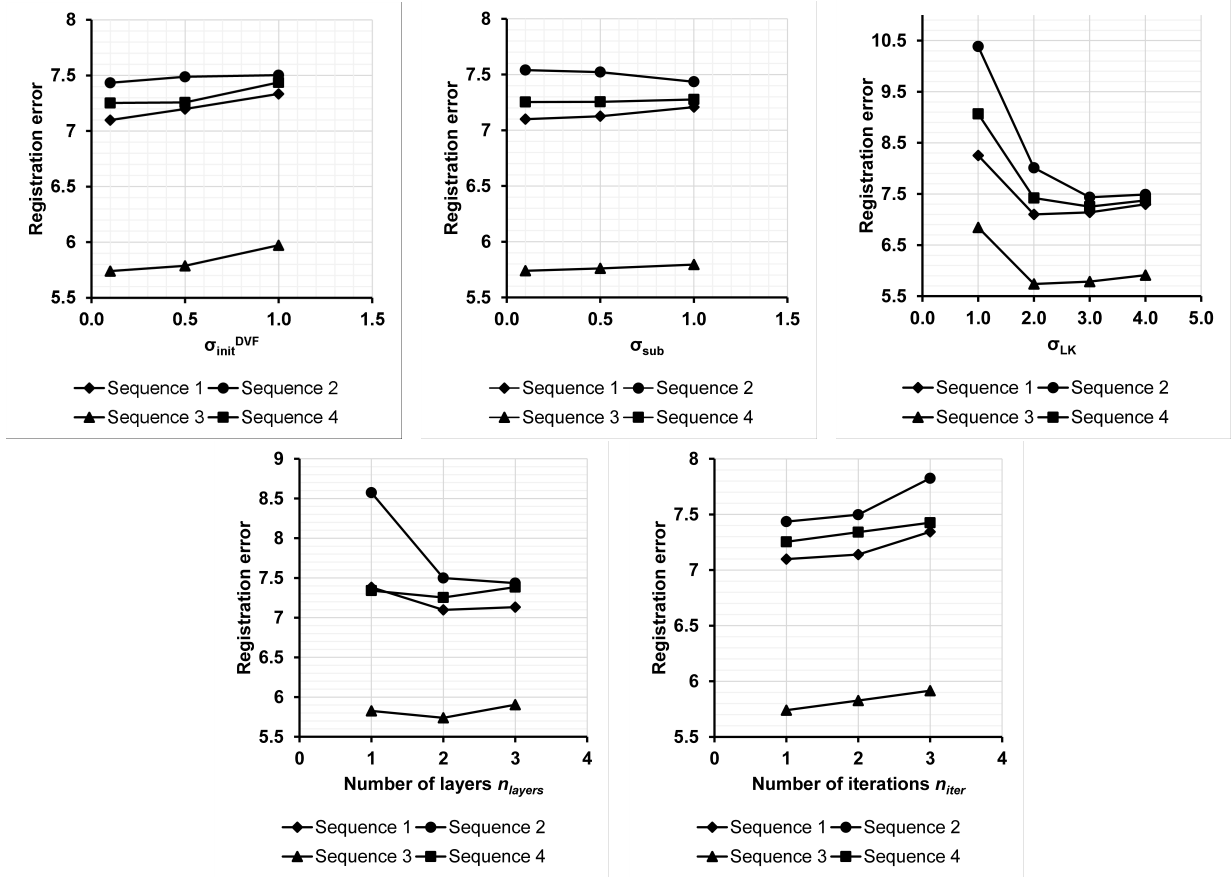


Figure 16: Registration error E_{gt} as a function of the parameters of the iterative and pyramidal version of the Lucas-Kanade optical flow algorithm. Given one parameter, each point in the associated graph corresponds to the minimum of E_{gt} over every possible combination of the other parameters in the grid (Table 6).

σ_{LK} , and setting $\sigma_{LK} = 1.0$ led to the worst performance. Moreover, as in [21], we found that using only one layer led to poor MRI registration due to the large amplitude of the respiratory motion relative to the (resampled) MR scan resolution (1mm^2 isotropic pixels). That aligns with the recommendation in the literature to use a multiresolution scheme to estimate the optical flow with chest scan images accurately [62, 68]. Similarly, a multi-scale approach based on a deep-learning encoder-decoder architecture was also used to predict spatial transformations in [46]. By contrast, an iterative approach was detrimental, as E_{gt} increased with n_{iter} in our experiments.

The normalized standard deviation of E_{gt} relative to each parameter is reported in Fig. 15. In the context of that figure, "normalization" means that the standard deviations associated with a particular sequence are multiplied by a common coefficient so that their sum equals 1. Similarly to the results on chest 4DCT in [21], σ_{LK} and n_{layers} were the parameters whose optimization contributed the most to minimizing E_{gt} with our 4D-MRI dataset, as their associated standard deviations were the highest (Fig. 15). Specifically, their optimization respectively led to a 19.6% and 5.4% decrease in the minimum registration error (Fig. 16).

B. Appendix : Notes on the PCA respiratory motion model

In this section, we explain how to derive the equations for the PCA motion model as described in Section 2.2 (Eqs. 2 and 3) from the original matrix description of the PCA algorithm. That model is subject-specific and similar to the original one proposed in [7], although, in our work, PCA is only applied to internal motion, and no surrogate data is involved. We first define a "data matrix" containing motion information for a given sequence until time step $M \in \mathbb{N}$ as follows:

$$X = \begin{bmatrix} u_x(\vec{x}_1, t_1) & u_y(\vec{x}_1, t_1) & u_x(\vec{x}_2, t_1) & \dots & u_y(\vec{x}_{|I|}, t_1) \\ & & \dots & & \\ u_x(\vec{x}_1, t_M) & u_y(\vec{x}_1, t_M) & u_x(\vec{x}_2, t_M) & \dots & u_y(\vec{x}_{|I|}, t_M) \end{bmatrix} \quad (12)$$

In the matrix above, $u_x(\vec{x}, t)$ and $u_y(\vec{x}, t)$ respectively refer to the x and y components of $\vec{u}(\vec{x}, t)$, the DVF at time t . We set M to be equal to the number of training images, i.e., $M = M_{train}$. We define the mean deformation $\mu_X \in \mathbb{R}^{1 \times 2P}$ as the line vector containing the mean of each column of X :

$$\mu_X = [\mu_x(\vec{x}_1), \mu_y(\vec{x}_1), \mu_x(\vec{x}_2), \dots, \mu_y(\vec{x}_{|I|})] \quad (13)$$

In that equality, $\mu_x(\vec{x}_i)$ and $\mu_y(\vec{x}_i)$ respectively refer to the average of $u_x(\vec{x}_i, t_k)$ and $u_y(\vec{x}_i, t_k)$ over $k \in \llbracket 1, \dots, M \rrbracket$. We then compute the centered data matrix X_c , whose column vectors each have a mean equal to 0, as follows:

$$X_c = X - \mathbb{1}_{M \times 1} \mu_X \quad (14)$$

Given an arbitrary integer $n_{cp} \in \mathbb{N}$, PCA enables finding two matrices, $W \in \mathbb{R}^{M \times n_{cp}}$ and $U \in \mathbb{R}^{2|I| \times n_{cp}}$, that minimize the quantity $\|X_c - WU^T\|_2$ subject to the two following conditions¹⁷:

- $W^T W$ is a diagonal matrix
- $U^T U = I_{n_{cp}}$ (identity matrix of size n_{cp})

Specifically, we first perform the spectral decomposition of $Y = X_c X_c^T$, i.e., we compute the matrix of eigenvectors V and diagonal matrix Λ that contains the square root of the eigenvalues, satisfying by definition:

$$Y = V \Lambda^2 V^T \quad (15)$$

We introduce the following notations:

$$\Lambda = \begin{bmatrix} \lambda_1 & & \\ & \ddots & \\ & & \lambda_M \end{bmatrix} \quad \text{with } \lambda_1 \geq \dots \geq \lambda_M \geq 0 \quad (16)$$

$$V = [V_1, \dots, V_M] \quad (17)$$

We multiply each column vector V_i by the sign of its first non-zero entry (which thereby becomes positive). We included that additional normalization step to make the PCA algorithm output consistent regardless of the eigendecomposition algorithm used¹⁸. The matrices W and U are computed using the first n_{cp} eigenvalues and eigenvectors as follows:

$$W = [V_1, \dots, V_{n_{cp}}] \begin{bmatrix} \lambda_1 & & \\ & \ddots & \\ & & \lambda_{n_{cp}} \end{bmatrix} \quad (18)$$

$$U = X_c^T [V_1, \dots, V_{n_{cp}}] \begin{bmatrix} 1/\lambda_1 & & \\ & \ddots & \\ & & 1/\lambda_{n_{cp}} \end{bmatrix} \quad (19)$$

U is the principal components matrix, and its columns are the principal components. W is referred to as the weight matrix. X , W , and U approximately satisfy the following relationship:

$$X - \mathbb{1}_{M \times 1} \mu_X = WU^T \quad (20)$$

¹⁷The PCA weight matrix W in this appendix is different from the matrix of coefficients in linear regression in Table 2.

¹⁸In particular, that normalization step ensures that the first non-zero (scalar) time-dependent weight is always positive for all $j \in \llbracket 1, \dots, n_{cp} \rrbracket$: $w_j(t_1) \geq 0$.

We denote the entries of W and U as follows:

$$W = \begin{bmatrix} w_1(t_1) & \dots & w_{n_{cp}}(t_1) \\ \dots & \dots & \dots \\ w_1(t_M) & \dots & w_{n_{cp}}(t_M) \end{bmatrix} \quad (21)$$

$$U = \begin{bmatrix} u_1^x(\vec{x}_1) & \dots & u_{n_{cp}}^x(\vec{x}_1) \\ u_1^y(\vec{x}_1) & \dots & u_{n_{cp}}^y(\vec{x}_1) \\ u_1^x(\vec{x}_2) & \dots & u_{n_{cp}}^x(\vec{x}_2) \\ \dots & \dots & \dots \\ u_1^y(\vec{x}_{|I|}) & \dots & u_{n_{cp}}^y(\vec{x}_{|I|}) \end{bmatrix} \quad (22)$$

Using the latter notations, we infer from Eq. 20 that for all pixel indices $i \in \llbracket 1, \dots, |I| \rrbracket$ and time step $k \in \llbracket 1, \dots, M \rrbracket$:

$$\begin{cases} u_x(\vec{x}_i, t_k) = \mu_x(\vec{x}_i) + \sum_{j=1}^{n_{cp}} w_j(t_k) u_j^x(\vec{x}_i) \\ u_y(\vec{x}_i, t_k) = \mu_y(\vec{x}_i) + \sum_{j=1}^{n_{cp}} w_j(t_k) u_j^y(\vec{x}_i) \end{cases} \quad (23)$$

These two latter equations can be combined and rewritten as Eq. 2 by defining $\vec{\mu}(\vec{x}_i) = [\mu_x(\vec{x}_i), \mu_y(\vec{x}_i)]^T$ and $\vec{u}_j = [u_j^x(\vec{x}_i), u_j^y(\vec{x}_i)]^T$. Eq. 2 is the explicit geometrical form of Eq. 20, the latter being expressed using a more abstract linear algebra framework. Both describe the PCA motion model, which approximates high-dimensional time-dependent deformation fields $\vec{u}(\vec{x}, t)$ by a linear combination of a few (static) independent vector fields $\vec{u}_j(x)$ generating a low-dimensional linear subspace, weighted by the time-dependent weights $w_j(t)$.

Similarly, the relationship $U^T U = I_{n_{cp}}$, which expresses the orthonormality of the principal components, is equivalent to Eq. 4. Using the same relationship, one can rewrite Eq. 20 as follows:

$$W = X_c U \quad (24)$$

For $k \in \mathbb{N}$, we define the following row vector, corresponding to the deformation field at time t_k , centered using the mean DVF of the training set:

$$X_c(t_k) = [u_x(\vec{x}_1, t_k), u_y(\vec{x}_1, t_k), u_x(\vec{x}_2, t_k), \dots, u_y(\vec{x}_{|I|}, t_k)] - \mu_X \quad (25)$$

$X_c(t_k)$ is the k^{th} row of the centered data matrix $X_c \in \mathbb{R}^{M_{train} \times 2|I|}$ when $k \leq M_{train}$. Eq. 24 can be rewritten as:

$$[w_1(t_k), \dots, w_{n_{cp}}(t_k)] = X_c(t_k) U \quad (26)$$

The latter equation expresses the fact that the time-dependent weights at time t_k can be computed by projecting the flattened centered DVF vector $X_c(t_k)$ onto the hyperplane of $\mathbb{R}^{2|I|}$ spanned by the (orthogonal) columns of U . During inference, we keep the principal components from

Prediction parameters	
Output layer size	$p = n_{cp}$
Input layer size	$m = n_{cp}L$
Number of hidden layers	1
Size of the hidden layer	q
Activation function ϕ	Hyperbolic tangent
Training algorithms	RTRL, UORO, SnAp-1, DNI
Optimization method	Stochastic gradient descent
Gradient clipping threshold	$\tau_{RNN} = 100$
Weights initialization	Gaussian $\mathcal{N}(0, \sigma_{init} = 0.02)$
Input data normalization	Yes (online)
Cross-validation metric to select RNN hyper-parameters	nRMSE (Eq. 7)
Cross-validation metric to select n_{cp}	Registration error $E_{pred}(n_{cp})$ (Eq. 10)
Number of runs for selecting the RNN hyper-parameters	$n_{cv} = 250$ (10 for RTRL)
Cross-validation range for n_{cp}	$n_{cp} \in \{1, 2, 3, 4\}$
Nb. of runs for selecting n_{cp}	$n_{warp} = 25$ (5 for RTRL)
Number of runs for evaluating image prediction test accuracy (in Section 3.4.1)	n_{warp} (same as previous row)
Nb. of runs for evaluating PCA weight prediction test accuracy (in Section 3.2.1)	$n_{test}^{PCA} = 250$ (10 for RTRL)
Last training time step index	$M_{train} = 90$ ($t_{M_{train}} = 28.26s$)
Last cross-val. time step index	$M_{cv} = 180$ ($t_{M_{cv}} = 56.52s$)
Test time interval	6.28s (20 time steps)

Table 7

Parameters related to the experimental setup and RNN configuration. n_{cp} and L designate the number of principal components and the SHL expressed in number of time steps, respectively. n_{cv} , n_{warp} , and n_{test}^{PCA} are lower for RTRL as the latter is slower and its associated errors have lower uncertainty, compared with the other RNN algorithms.

the training data and define the weights as the projection of the centered DVF $X_c(t_k)$ computed from the incoming data onto the same hyperplane. In other words, Eq. 26 is also valid for $k > M_{train}$. Fig. 1 illustrates the projection idea described above. Eq. 3 can simply be derived from Eq. 26 and expresses the latter with a different viewpoint.

C. Appendix: RNN experimental setup

Table 7 outlines the parameters related to the cross-validation and RNN configuration in our research.